Cell

Passage of the HIV capsid cracks the nuclear pore

Graphical abstract

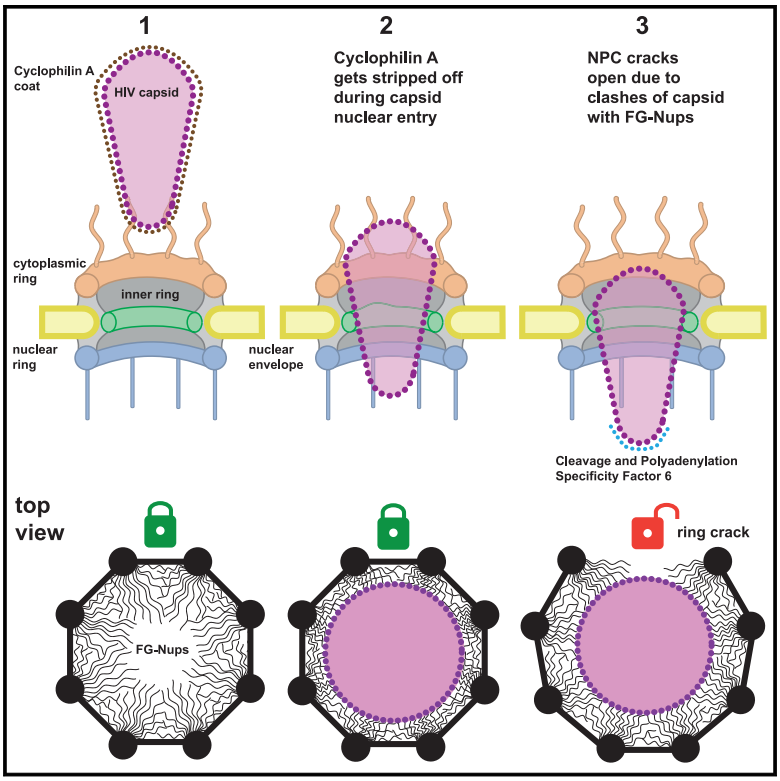

Highlights

- Cone-shaped HIV-1 capsids accumulate at and pass through nuclear pores in macrophages
- The capsid lattice remains largely intact during nuclear entry
- Nuclear pores can crack open upon passage of the HIV-1 capsid
- Nuclear pore cracking may relieve steric blockage of HIV-1 capsid

Authors

Jan Philipp Kreysing, Maziar Heidari, Vojtech Zila, ..., Gerhard Hummer, Hans-Georg Kräusslich, Martin Beck

Correspondence

gerhard.hummer@biophys.mpg.de (G.H.), hans-georg.kraeusslich@med.uni-heidelberg.de (H.-G.K.), martin.beck@biophys.mpg.de (M.B.)

In brief

Cone-shaped HIV-1 capsids with largely intact lattices accumulate at and pass through nuclear pores in primary human macrophages. The nuclear pores can crack open upon passage of the HIV-1 capsid, possibly to relieve a steric blockage of capsids inside pores.

Kreysing et al., 2025, Cell *188*, 1–14
February 20, 2025
https://doi.org/10.1016/j.cell.2024.12.008

CellPress

Cell

CellPress
OPEN ACCESS

Article

Passage of the HIV capsid cracks the nuclear pore

Jan Philipp Kreysing,[1,2,10] Maziar Heidari,[3,10] Vojtech Zila,[4,9,10] Sergio Cruz-León,[3] Agnieszka Obarska-Kosinska,[1] Vibor Laketa,[4,5] Lara Rohleder,[4] Sonja Welsch,[6] Jürgen Köfinger,[3] Beata Turoňová,[1] Gerhard Hummer,[3,7,*] Hans-Georg Kräusslich,[4,5,*] and Martin Beck[1,8,11,*]

[1]Department of Molecular Sociology, Max Planck Institute of Biophysics, Max-von-Laue-Straße 3, 60438 Frankfurt am Main, Germany
[2]IMPRS on Cellular Biophysics, Max-von-Laue-Straße 3, 60438 Frankfurt am Main, Germany
[3]Department of Theoretical Biophysics, Max Planck Institute of Biophysics, Max-von-Laue-Straße 3, 60438 Frankfurt am Main, Germany
[4]Department of Infectious Diseases, Virology, Heidelberg University, Heidelberg, Germany
[5]German Centre for Infection Research (DZIF), Partner Site Heidelberg, Heidelberg, Germany
[6]Central Electron Microscopy Facility, Max Planck Institute of Biophysics, Max-von-Laue-Straße 3, 60438 Frankfurt am Main, Germany
[7]Institute of Biophysics, Goethe University Frankfurt, 60438 Frankfurt am Main, Germany
[8]Institute of Biochemistry, Goethe University Frankfurt, 60438 Frankfurt am Main, Germany
[9]Present address: AskBio GmbH, 69123 Heidelberg, Germany
[10]These authors contributed equally
[11]Lead contact
*Correspondence: gerhard.hummer@biophys.mpg.de (G.H.), hans-georg.kraeusslich@med.uni-heidelberg.de (H.-G.K.), martin.beck@biophys.mpg.de (M.B.)
https://doi.org/10.1016/j.cell.2024.12.008

SUMMARY

Upon infection, human immunodeficiency virus type 1 (HIV-1) releases its cone-shaped capsid into the cytoplasm of infected T cells and macrophages. The capsid enters the nuclear pore complex (NPC), driven by interactions with numerous phenylalanine-glycine (FG)-repeat nucleoporins (FG-Nups). Whether NPCs structurally adapt to capsid passage and whether capsids are modified during passage remains unknown, however. Here, we combined super-resolution and correlative microscopy with cryoelectron tomography and molecular simulations to study the nuclear entry of HIV-1 capsids in primary human macrophages. Our data indicate that cytosolically bound cyclophilin A is stripped off capsids entering the NPC, and the capsid hexagonal lattice remains largely intact inside and beyond the central channel. Strikingly, the NPC scaffold rings frequently crack during capsid passage, consistent with computer simulations indicating the need for NPC widening. The unique cone shape of the HIV-1 capsid facilitates its entry into NPCs and helps to crack their rings.

INTRODUCTION

Human immunodeficiency virus type 1 (HIV-1) is a lentivirus that can infect non-dividing cells, including macrophages.[1] Following cytoplasmic entry of the characteristic cone-shaped HIV-1 capsid, the viral genomic RNA is reverse transcribed into double-stranded cDNA, which eventually becomes integrated into the host cell genome. Reverse transcription initiates in the cytoplasm and is completed after nuclear entry and prior to integration.[2–4] HIV-1 subviral complexes comprise the viral genome associated with nucleocapsid proteins, reverse transcriptase (RT), and integrase (IN). While earlier studies indicated rapid disassembly in the cytoplasm, it is now clear that the capsid can be stably maintained up to nuclear entry.[5,6] During cytoplasmic transit, HIV-1 capsids serve as reaction containers for reverse transcription and shield nascent viral cDNA from cytoplasmic DNA sensors.[5,6] Furthermore, the capsid lattice engages microtubular motors, thus facilitating its transport toward the nuclear envelope (NE).[7–9] It also interacts with cytoplasmic cyclophilin A (CypA)[10,11] and with the Cyp domain of Nup358 at the cytoplasmic side of nuclear pore complexes (NPCs), potentially docking the capsid to the NPC.[12]

The HIV-1 capsid consists of 200–250 hexamers of the viral CA (capsid) protein with 12 CA pentamers inserted in regions of high curvature.[13–15] CA hexamers specifically bind phenylalanine-glycine (FG) repeats within intrinsically disordered regions of several nucleoporins (FG-Nups),[16,17] and the same hydrophobic cleft in the CA hexamer interacts with an FG-containing motif of nuclear cleavage-and-polyadenylation-specificity-factor 6 (CPSF6).[17] FG-motif-containing host factors can be displaced by competitive binding of small molecules (e.g., Lenacapavir, recently approved for treatment of HIV-1-infected patients[18,19]). These capsid-targeting compounds block nuclear entry of HIV-1 replication complexes, supporting a role of the capsid during NPC passage.[16,19,20] The size discrepancy between the HIV-1 capsid (ca. 60 nm at the broad end[15]) and the inner NPC diameter measured in isolated NEs (ca. 45 nm[21]), and the perceived inherent instability of the CA lattice (before stabilization through IP6 was discovered[22]), had led to the conclusion that genome uncoating must occur prior to NPC channel entry. This

Please cite this article in press as: Kreysing et al., Passage of the HIV capsid cracks the nuclear pore, Cell (2025), https://doi.org/10.1016/j.cell.2024.12.008

hypothesis was supported by the observation that a CypA-DsRed fluorescent fusion protein, which efficiently binds cytoplasmic capsids, was rapidly lost when the structure reached the nuclear pore.[23] Recent ultrastructural studies have shown, however, that (largely) intact capsids can enter the nucleus in a T cell line through apparently normal nuclear pores,[24] and nuclear cone-shaped capsids encasing electron-dense nucleoprotein complexes were also detected in other cell types.[4,24,25] Recently, NPC central channel diameters were shown to adapt in response to laterally imposed forces,[26] and their inner diameter of approximately 45–65 nm[24,27–29] in human tissue culture cells appeared sufficiently wide for passage of the complete HIV-1 capsid.

NPCs consist of three sandwiched rings. The nuclear (NR), inner (IR), and cytoplasmic ring (CR) are 8-fold rotationally symmetric structures that form a central channel, thus bridging across the inner and outer membranes of the NE. While the CR and NR form an elaborate and thoroughly connected scaffold that is bent during dilation movements, the IR consists of eight spokes that are flexibly connected. These spokes move outward and away from each other during NPC dilation, thereby stretching their linkers and opening up additional space within the central channel.[27,30] If and how the dilation of individual NPCs is coordinated with large cargo transport remains unknown. Nuclear transport receptor-bound cargo passes through the central channel, which is filled with tens of megadaltons of intrinsically disordered FG-Nups. FG-Nups selectively bind receptor-bound cargo to facilitate nuclear import but at the same time preclude nuclear entry of the vast majority of proteins.[31] FG-Nups thus form the NE permeability barrier, protect the host cell genome, and constitute a major barrier that HIV-1 capsids have to overcome for nuclear entry.[32] Two recent studies showed that *in vitro*-assembled HIV-1 capsids rapidly partitioned into phase-separated condensates of an intrinsically disordered FG repeat region, which was dependent on the FG-binding pocket in CA.[33,34] These results confirmed that the viral capsid constitutes a multivalent nuclear import receptor.

The two central questions regarding nuclear import of the HIV-1 capsid are how do capsids pass through a channel of comparable width that is densely filled with FG-Nups? And at what location do capsids open to release the viral genome? Three non-mutually exclusive scenarios may be considered: (1) the capsid lattice may be elastic, a hypothesis supported by a study reporting reversible capsid deformation without disintegration.[35] (2) The capsid lattice may break during NPC passage, thus altering its geometry. While morphologically normal-appearing capsids were detected in the nucleoplasm of non-dividing cells, lattice completeness of intracellular capsids has not been determined. (3) Passage of the HIV-1 capsid through the NPC channel may induce local NPC dilation, possibly to a point where the NPC scaffold is altered.

Here, we show that NPC passage appears rate-limiting in primary human macrophages and identify apparently intact, nucleic acid-containing capsids in the nucleoplasm of these cells. Most importantly, we provide evidence that passage of intact HIV-1 capsids cracks the NPC scaffold. Computational simulation supports a scenario in which cracking of the NPC scaffold facilitates capsid passage by relieving a steric barrier.

RESULTS

Subviral HIV-1 complexes accumulate at nuclear pores in human primary macrophages

We studied nuclear entry of subviral HIV-1 complexes in human primary monocyte-derived macrophages (MDMs). Macrophages are natural target cells of HIV-1 and are postmitotic. Accordingly, the viral replication complex has to enter the nucleus through the intact NE. To analyze this process, we made use of our previously described non-infectious HIV-1 variant (NNHIV) that enters permissive cells normally and undergoes reverse transcription and nuclear entry but is defective in integration and gene expression.[24]

Freshly prepared MDMs were incubated with NNHIV carrying a macrophage-tropic HIV-1 glycoprotein, and fixed cells were immunostained for HIV-1 CA and lamin A/C (nuclear boundary). The efficiency of subviral complexes to reach the nucleus varied significantly between individual cells from one donor as well as between different donors. Analyzing 77 MDMs from four different donors that had been incubated with NNHIV, we observed a total of 3,815 CA signals, of which 323 were nuclear (range 0–12 per cell) and 1,665 were at the NE (range 0–103 per cell). Twenty-four cells showed 30 or more CA signals at the NE. This phenotype was detected at 24 h post infection (p.i.) and increased at 48 h p.i. (Figures 1A–1C), while CA signals were cytoplasmically distributed at earlier times. Starting at 24 h p.i., we observed HIV-1 signals in the nucleus, and their number increased at 48 h p.i. (Figures 1A–1C).

To analyze whether NE-associated capsids were enriched at NPCs, we performed two-color 3D stimulated emission depletion (3D STED) nanoscopy. MDMs were incubated with NNHIV for 48 h, stained for HIV-1 CA and FG-Nups, and super-resolved images acquired in sequential optical sections to cover the entire nuclear volume of individual cells. Analysis of computational slices of four fully reconstructed MDM nuclei confirmed the direct association of HIV-1 capsids with NPCs (Figure 1D; Video S1). Quantitative analysis showed that 89% (908 of 1,025) of CA signals detected at the NE were closely associated with NPCs, with an average of 17% of all NPCs associated with a viral capsid. This strong accumulation further supported the notion that passage through the nuclear pore is a rate-limiting event in early HIV-1 replication.[36]

HIV-1 capsids are detected upon entry into, passage through, and exit from the NPC

To determine the relative positioning of HIV-1 capsids at NPCs, we performed two-color STED nanoscopy for CA and FG-Nups. Maximum intensity of the FG repeat signal is expected to localize to the central channel at the NPC IR.[37] At 48 h p.i., we observed CA signals in three positions: at the cytoplasmic side, directly overlapping the FG signal, and at the nucleoplasmic side of the nuclear pore (Figure 2A). For quantitative analysis, we segmented individual capsid-associated NPCs and determined the normalized signal intensities of the FG-Nup and CA signals for a line profile (Figure 2B). This confirmed that HIV-1 capsids could be observed upon their entry into, passage through, and exit from the central NPC channel. The distribution of these three positions relative to the center of the NPC was determined for a total of 180

Please cite this article in press as: Kreysing et al., Passage of the HIV capsid cracks the nuclear pore, Cell (2025), https://doi.org/10.1016/j.cell.2024.12.008

CellPress
OPEN ACCESS

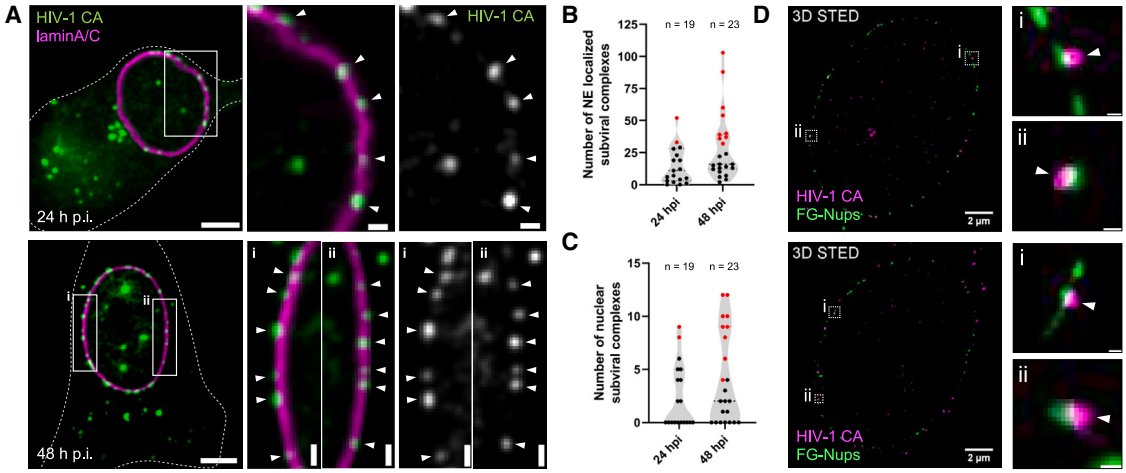

Figure 1. HIV-1 capsids accumulate at NPCs in MDM

(A–C) MDMs were infected with NNHIV for 24 h (A, upper) or 48 h (A, lower) and stained for HIV-1 CA (green) and lamin A/C (magenta). Shown are confocal z slices, and dashed lines mark cell boundaries. Enlarged regions (A, center, right) display HIV-1 CA signals (white arrowheads) accumulated at the NE as defined by lamin A/C staining. Scale bars: 5 μm (overviews), 1 μm (enlargements). (B and C) Quantification of CA signals representing subviral complexes colocalizing with lamin A/C (B) and number of CA signals detected inside the nucleus (C) at indicated times p.i. Cells exhibiting >30 CA signals colocalizing with lamin A/C in red. Results represent data obtained by analysis of (*n*) cells from one representative donor.

(D) 3D STED imaging of HIV-1-infected MDM nuclei stained for HIV-1 CA (magenta) and FG-Nups (green). Slices through the 3D reconstruction of an entire nucleus are shown with enlargements (D, right) displaying CA signals (white arrowheads) directly associated with NPCs as defined by FG-Nup staining. See also Video S1. Scale bars: 2 μm (overviews), 100 nm (enlargements).

capsid-associated NPCs in MDMs from three different donors (Figure 2C). A similar distribution was observed for all three donors, with 51% of capsids observed on the cytoplasmic side, 33% overlapping the FG repeats in the central channel, and 15% on the nucleoplasmic side of the NPC (Figure 2C).

Subviral complexes passing through the central NPC channel are cone-shaped capsids

Fluorescence imaging clearly revealed CA-containing subviral complex accumulation at and inside NPCs of infected MDMs but did not provide sufficient resolution to define the morphology and structure of these complexes. We therefore applied 3D correlative light and electron microscopy (CLEM). MDMs infected with NNHIV carrying a fluorescent fusion protein of the viral IN with mScarlet to identify intracellular HIV-1 complexes were cryo-immobilized by high-pressure freezing at 48 h p.i. and further processed for CLEM. Tilt series were acquired for 61 positions of correlated regions targeting IN.mScarlet signals at NE regions (defined by Hoechst staining) in 17 cells from two donors. We identified 43 structures completely covered in the resin sections that resembled HIV-1 capsids inside or immediately adjacent to NPCs. Their distribution across the NPC was similar to that observed by STED nanoscopy with 19 subviral particles on the cytoplasmic side, 13 deep inside the NPC, and 11 on the nucleoplasmic side (Figure S1). The morphology of subviral structures closely matched that of mature capsids in HIV-1 particles, including dense material inside capsid structures indicating the presence of condensed ribonucleoprotein or reverse transcription intermediates (Figures 3 and S1). The majority of structures was cone-shaped (41/43; 95%) with rare tubular structures (2/43; 4.7%) (Figure S1). Capsid-like structures at or within the NPC exhibited an average length of 111 ± 11 nm and an average width of 53 ± 6 nm, similar to mature HIV-1 capsid dimensions determined by cryoelectron tomography (cryo-ET) of viral particles[38] and almost identical to the dimensions observed in our previous CLEM analysis of an infected T cell line.[24] We did not observe apparently empty (lacking dense inner material) or obviously broken capsid-like particles inside or directly associated with the NPC in infected MDMs (Figure S1).

Figure 3A depicts CLEM of a strongly fluorescent cluster associated with the nuclear border of an infected MDMs. A slice through the tomographic reconstruction at the correlated position is shown in Figure 3A″. The segmented and isosurface-rendered representation of this region (Figure 3A‴) features a total of five cone-shaped and visually intact HIV-1 capsids completely covered in the resin section. Three of these had entered the central channel with their narrow end first and were captured at different stages of nuclear import (inserts i, ii, iii in Figures 3A″ and 3A‴ and Video S2). Another capsid (iv in Figure 3A‴) localized close to the CR of the NPC with its narrow end oriented toward the NPC, and this orientation was also observed in all 32 capsids inside the channel (Figure S1). Capsids positioning their broad end toward the NE were detected in the vicinity of NPCs (Figure 3A‴ capsid v), but not for particles that had entered into the channel. Capsid-like structures deep inside the central channel (Figure 3A) and on the nucleoplasmic side (Figures 3B and 3C) retained apparently normal cone-shaped morphology (except for one tubular structure) and dense material inside without any obvious defects (Figure S1). Contrary to expectation, capsids on the nucleoplasmic side were found in two orientations with equal frequency: with their narrow end away from (Figure 3B, inset ii) or toward the NPC (Figures 3C and S1).

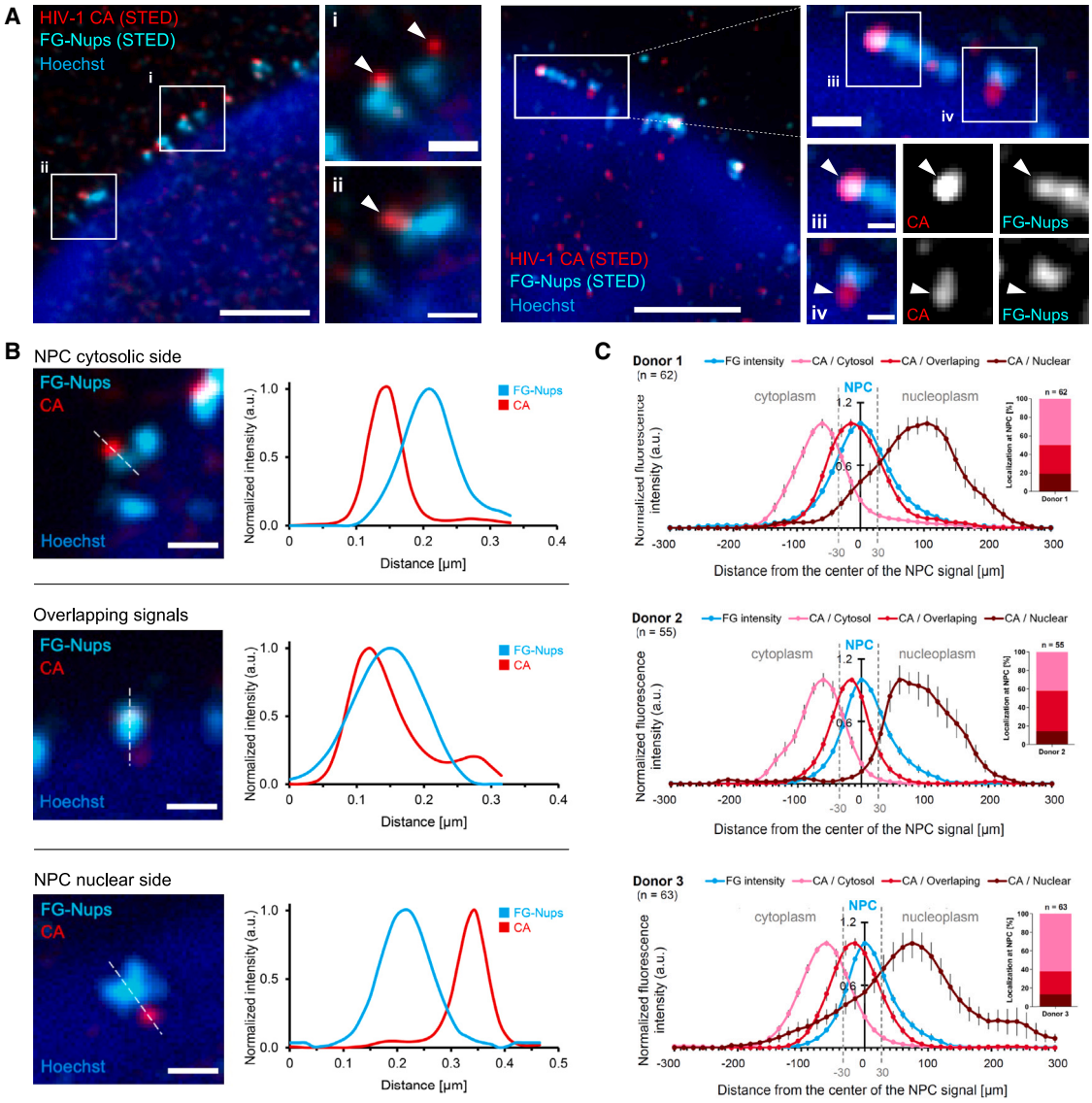

Figure 2. Super-resolution analysis of HIV-1 subviral complexes at nuclear pores of infected MDMs

MDMs were infected with NNHIV, fixed 48 h p.i., and immunostained for HIV-1 CA (red) and FG-Nups (cyan). The nuclear side (Hoechst) was identified in confocal mode (blue).

(A) STED microscopy displaying two infected MDMs. The enlarged regions show CA signals (white arrowheads) at the cytoplasmic side of the NPC (i and ii), overlapping CA and NPC signals (iii), and CA signals at the nuclear side of the NPC (iv). Scale bars: 1 µm (overviews), 200 nm (enlargements i, ii, upper right), 100 nm (enlargements iii, iv).

(B) Three typical localizations of HIV-1 signals at the NPC with corresponding CA and FG-Nup signal intensity profiles. Graphs show intensities normalized to the respective maximal value measured in line profiles indicated in images on the left. Scale bars: 200 nm.

(C) Averaged line profiles measured on (*n*) NPCs with associated CA signals in MDMs from three different donors. Error bars represent SD. The localization of CA signals at the NPC was classified as cytoplasmic side of the NPC (pink line), overlapping with NPC (red line) or nuclear side of the NPC (dark red line), applying a window of 30 nm distance of the CA intensity peak from the FG-Nup (magenta line) intensity peak (dashed vertical lines).

The CypA binding site is occupied on cytosolic capsids

To investigate the capsid structure and its interaction with NPCs in more detail, we used cryo-ET. We subjected NNHIV-infected and uninfected MDMs to specimen thinning by focused ion beam (FIB) milling and acquired 96 and 52 tilt series, respectively (Figure S2; Table S1). In the reconstructed tomograms, we identified 13 enveloped particles outside and 36 capsids inside cells, the latter either in the cytosol, nucleoplasm, or NPC-associated (Figure 4; see also Video S3), and ten of these capsids were located in direct proximity or inside NPCs (Figure 5B). These capsids appeared morphologically intact, and the large majority displayed interior density as typically observed for the nucleoprotein complex.

We used subtomogram averaging (STA) of capsid surfaces as previously described[15,40] to structurally analyze the capsid

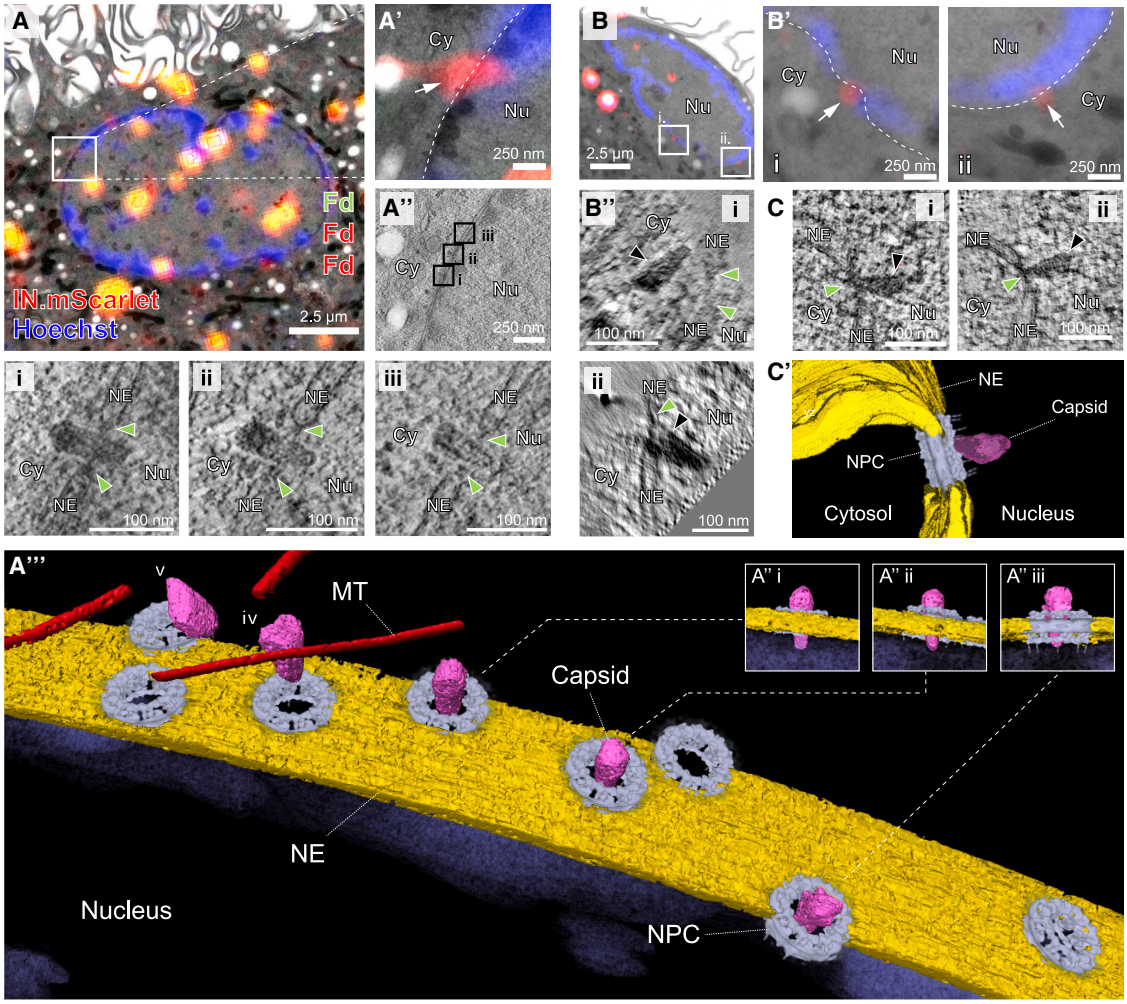

Figure 3. Morphologically intact HIV-1 capsids at and inside NPCs of human MDMs

MDMs were infected with IN.mScarlet carrying NNHIV for 48 h at 37°C. Fluorescently labeled subviral structures in the NE region were visualized by CLEM-ET. Dashed lines in enlargements outline the NE.

(A and A′) CLEM overlay (A) with enlargement (A′) showing positions of IN.mScarlet signals (red; white arrow) at the NE in an EM section post-stained with Hoechst (blue) and decorated with multi-fluorescent fiducials (Fd) for correlation.

(A″) Slice through a tomographic reconstruction at the correlated position shown in (A) and (A′). The features i–iii shown enlarged in the bottom panel represent capsids that deeply penetrate the central NPC channel (green arrowheads). Cy, cytosol; Nu, nucleus; NE, nuclear envelope; NPC, nuclear pore complex.

(A‴) Same as in (A″) but displayed segmented and isosurface rendered. MT (microtubule), red; capsid, magenta; NE, yellow; NPC, gray (downsampled cryo-ET map from this study). NPC isosurfaces were artificially inserted and have not originated from this tomography dataset. Capsids i–iii as in (A″), capsid iv associated with a microtubule (as described previously[24]), and capsid v at the NE but away from NPCs. See also Video S2.

(B and B″) Depict CLEM and enlargement as in (A) and (A″), showing capsid docking at the NPC (i) and capsid located in the nuclear basket region (ii) from the same resin section. Both capsids display a conical shape and a dense interior (black arrowheads).

(C) Slices through tomographic reconstructions from different resin sections, showing two cone-shaped capsids in the NPC basket region oriented with their narrow ends toward the NPC density. Both capsids display a dense interior.

(C′) Same as in (C, inset i) but displayed segmented and isosurface rendered.

See also Figure S1.

lattice *in situ*. This analysis to a large extent identified the expected hexagonal signature of the lattice as well as CA pentamers from capsids inside virions, in the cytoplasm and inside the central NPC channel (Figure 4B). The lattice was clearly detectable in nuclear capsids as well, but it appeared overall less complete (Figure 4B). Whether the local differences in the nucleoplasm are caused by reduced contrast due to molecular crowding or, alternatively, by partial loss of capsid integrity cannot be judged at present.

To determine whether the CA lattice is decorated by different binders during its journey, we categorized the subtomograms according to subcellular localization of the capsid. As expected, structures of CA hexamers and pentamers in extracellular enveloped particles were very similar to previous studies[15] (Figures 4C

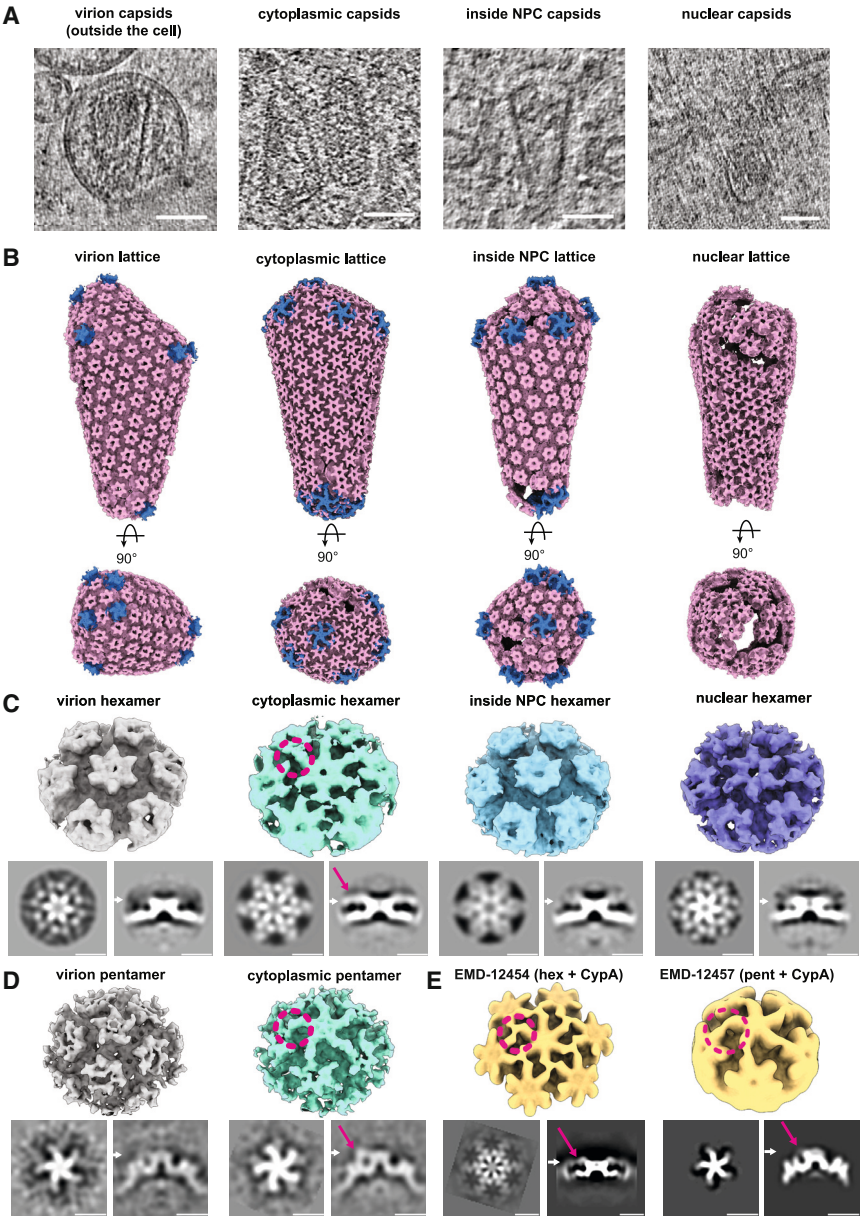

Figure 4. CA lattice is detected in the cytoplasm, during and post nuclear entry

(A) Virtual slices through cryo-tomograms of HIV-1 capsids inside virions, in the cytoplasm, inside NPCs, and in the nucleus.

(B) Capsid lattice traced by STA of CA hexamers. Capsids are displayed in a side view and a top view on the wide end. Respective subtomogram averages are shown in pink for hexamers and in blue for pentamers. The positions of pentamers were inferred from the hexagonal lattice, where possible, and subsequently subjected to STA. For capsids inside of NPCs, the number of detectable pentamers was insufficient for independent STA. Instead, pentamers were combined with those from cytoplasmic capsids.

(C) STA of the HIV-1 CA hexamer for virion (gray), cytoplasmic (mint), inside NPC (light blue), and nuclear capsids (purple) shows additional density between individual CA hexamers only for the cytoplasmic average (magenta circle and arrow). The map resolutions (ranging from 28 to 33 Å) and particle numbers are reported in Table S1.

(D) STA of the HIV-1 CA pentamer for virion (gray) and cytoplasmic (mint) shows additional density between the central CA pentamer and its neighbors for the cytoplasmic average (magenta circle and arrow).

(E) Published *in vitro* structures of CA hexamer and pentamer with CypA bound (EMDB: EMD-12454 and EMDB: EMD-12457, respectively,[39] both yellow) are shown lowpass filtered to 25 Å with the CypA density highlighted (magenta circle and arrow).

For (C)–(E), in addition to the isosurface representation, a top and side view slice through the density is shown (white arrow in the side view pointing to corresponding plane in the top view). Scale bar in (A): 50 nm, in (C)–(E): 10 nm.

See also Figure S2 and Videos S3 and S4.

and 4D). In cytosolic capsids, hexamers and pentamers were also clearly detected, but their structure contained additional density consistent with published *in vitro* structures of CypA bound to CA[11,39] (Figures 4C–4E). The respective density was strongly reduced in subtomogram averages obtained from capsids inside the central NPC channel (Figure 4C), supporting a model in which CypA is bound to the majority of CA hexamers in the cytosol and detached from the capsid upon NPC entry.

The NPC scaffold in macrophages is wider than most capsids

Previous STA analysis in a T cell line pointed to an overall dilated (64 nm at the IR) but otherwise normal three-ringed NPC architecture, both in infected and control cells, and the diameter of capsid-engaged NPCs was within the overall observed range.[24] However, these capsids contained the A77V mutation, which is defective in CPSF6 binding, and the result was based on a small number of capsids inside NPCs. It has been argued that capsids may induce additional NPC widening in order to pass through the central channel,[41] and this is best studied in postmitotic primary cells. We therefore subjected 200 and 118 NPCs from MDMs infected with or without NNHIV to STA. The resulting overall NPC structure was reminiscent of previous analyses in Hek293 and SupT1 cells[24,27] (Figures S3A and S3B). No obvious structural differences were apparent between NPCs from MDMs incubated with or without NNHIV, nor was their NPC diameter significantly different at the IR (Figures S3B and S3C). NPCs in MDMs were on average wider than in the previously analyzed SupT1 cells[24] (Figure S3D). Their IR displayed a more variable diameter compared with the CR and NR, consistent with the fact that IR spokes are flexibly connected.[27] At the observed inner diameter of the scaffold (~65 nm, Figure S3D),

Please cite this article in press as: Kreysing et al., Passage of the HIV capsid cracks the nuclear pore, Cell (2025), https://doi.org/10.1016/j.cell.2024.12.008

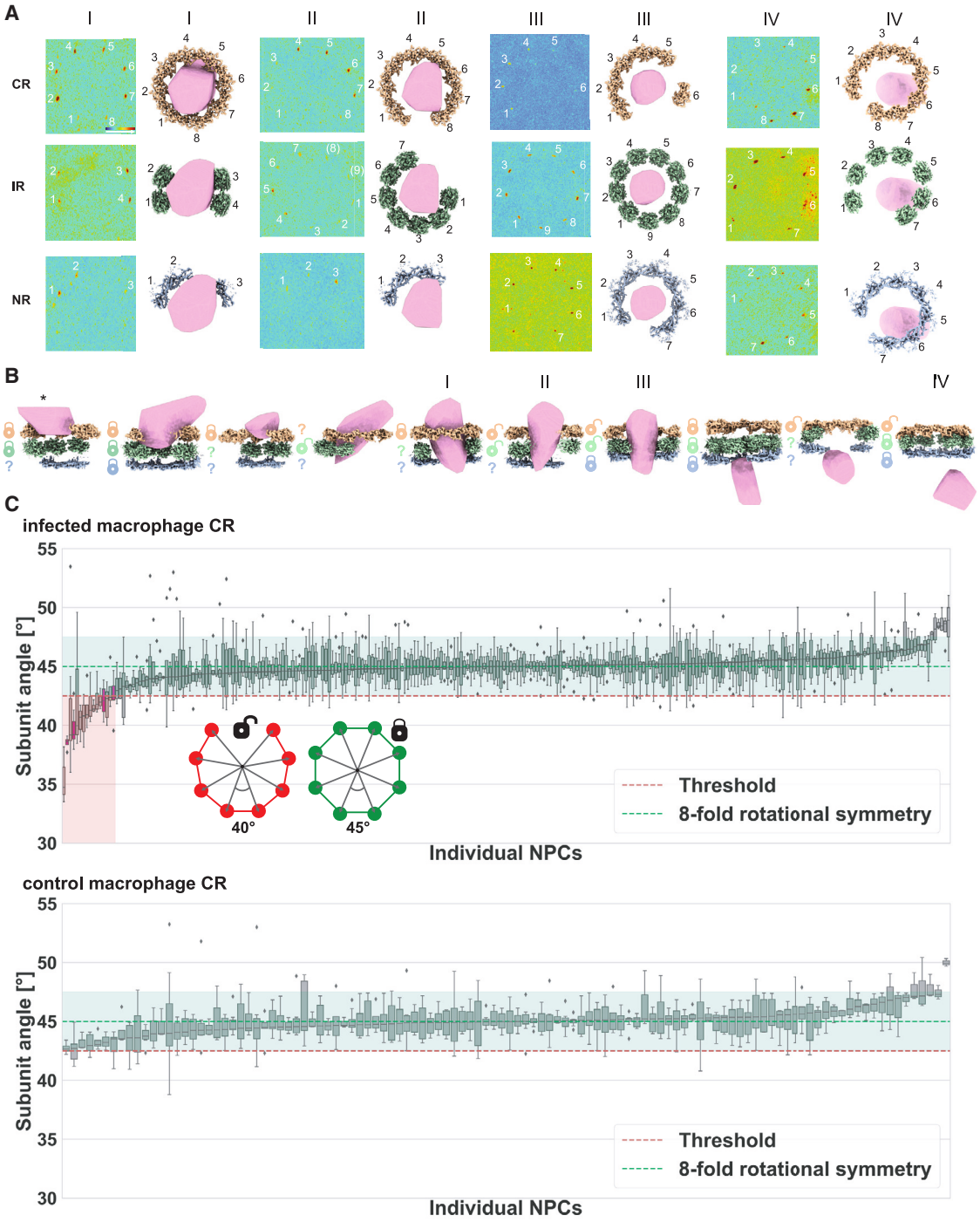

Figure 5. The presence of HIV-1 capsids inside the NPC is linked to abnormal NPC subunit arrangements

(A) Template matching results for subunits of CR (light orange, top), IR (green, middle), and NR (blue, bottom) for four NPCs associated with an HIV-1 capsid (surface rendering, pink). For each NPC, a maximum intensity projection of the constrained cross-correlation (CCC) volume with peaks for that ring subunit is shown color-coded (low: blue; high: red). Subunit arrangements are indicated in the right panels.

(B) Cross section gallery of NPCs sorted according to capsid position. The locks represent the status of that ring as either being unperturbed (closed lock) or cracked, i.e., inconsistent with canonical 8-fold rotational symmetry (open lock). This assignment is based on the IAOP (see STAR Methods for details) and a threshold of 42.5°. The asterisk denotes a case where the capsid is only partially contained in the tomographic volume. Question marks represent cases where the number of detected subunits was insufficient for assignment (less than three angle measurements). For the infected MDM dataset, NPCs without associated capsid were C8-symmetric 247 times and had cracked CR rings twelve times. NPCs with associated capsid were significantly more often cracked (Fisher's exact test, $p = 0.0009$; four out of nine cracked CR rings).

(legend continued on next page)

Please cite this article in press as: Kreysing et al., Passage of the HIV capsid cracks the nuclear pore, Cell (2025), https://doi.org/10.1016/j.cell.2024.12.008

the NPC would appear wide enough to accommodate most HIV-1 capsids with an average diameter of ~60 nm at their wide end (Figure S2F). To which extent the bulk of FG-Nups contributes to the effective diameter could not be estimated, however, because this analysis emphasizes scaffold Nups, while FG-Nups are averaged out.

Nuclear pores crack upon passage of the HIV-1 capsid

Recent advances in template matching allowed us to identify individual NPC subunits.[42,43] To structurally analyze the scaffold of capsid-engaged NPCs, we used individual subunits of the CR, IR, and NR for template matching, as previously described.[43] Visual inspection of the constrained cross-correlation (CCC) volumes revealed that five out of the ten capsid-engaged NPCs had a distorted scaffold, in which subunit positioning was not entirely in agreement with the canonical 8-fold rotational symmetry (Figures 5A and 5B). These distortions were not homogeneously distributed across the ring but rather at a specific position where the interior angle of the polygon (IAOP) (cartoon in Figure 5C), i.e., the rotation around the symmetry axis from a given to the neighboring subunit, was increased. Concomitantly, this angle was compressed for remaining subunits, thus indicating a rupture event that had cracked the ring structure of the scaffold. Such cracking events were only observed for NPCs in which the capsid had penetrated considerably into the central channel, but not in the three NPCs engaged by capsids at the cytosolic face of the NPC. In two NPCs with a capsid deep in the central channel, template matching indicated nine subunits of the IR (Figures 5AII, 5AIII, and S3E; Video S4). More frequently, however, ring cracking events co-occurred with apparent subunit losses. These were also observed in NPCs that showed a capsid associated with the nuclear face, indicative of damage induced during nuclear entry of this capsid.

NPC cracking is specific to infected macrophages

Nuclear entry of HIV-1 is rare. To determine statistical significance, we turned to an objective metric to quantify the number of cracking events in each of the three NPC rings. We defined NPC ring cracking based on the compression of the IAOP of the majority of subunits of a given NPC (Figure 5C). Using this sensitive assay, we confirmed that NPCs with exactly eight subunits had the expected IAOP sum of 360° (mean = 360.2°). Then, we asked whether capsid-engaged NPCs were more likely to display ring cracking compared with NPCs not associated with a capsid. This was the case (Fisher's exact test, $n = 268$, $p = 0.0009$ for the CR; see legend of Figure 5 for values). We furthermore showed that cracking occurred more frequently in NPCs in infected than control cells, regardless of whether a capsid was found in proximity of the respective NPC (Figure 5C) (for CR: Fisher's exact test, $p = 0.0043$; 252 C8-symmetric and 16 cracked rings in infected MDMs; 112 C8-symmetric and zero cracked rings in control MDMs). At the chosen angular threshold, no cracking events of the CR were observed in non-infected cells (Figure 5C), and they were rare at the level of the IR and NR in these cells (Figure S4).

These observations would also be expected if exceptionally large capsids were trapped at NPCs and induced damage while normal-sized capsids progressed faster into the nucleus and were invisible to our analysis. We therefore analyzed whether the mean size of capsids associated with nuclear pores exceeded that observed for enveloped particles outside of cells. This was not the case (Figure S2F).

HIV-1 capsids clash with NPC scaffolds in MD simulations

Each CA hexamer in the HIV-1 capsid can be bound by six of ~6,000 FG repeats. However, the balance between the resulting force pulling the capsid into the central channel and the counter-forces from displacing the bulk FG-Nups and clashes with the NPC scaffold remains unclear. Molecular dynamics (MD) simulations in combination with fluorescence resonance energy transfer (FRET) measurements of FG-Nups have recently shed light on their conformational dynamics *in situ*.[44] Here, we adapted this simulation framework to analyze the steric requirements for nuclear entry of HIV-1 capsids, the response of the FG-Nup network, and the associated forces.

We performed coarse-grained MD simulations to gain a detailed view of HIV-1 capsid passage through intact, dilated, and cracked NPCs with and without FG-Nups. We first built an atomic model of a typically sized cone-shaped HIV-1 capsid by completing its well-resolved fullerene-like lattice of CA hexamers and pentamers (Figures S5A and S5B). We then built a model of the dilated (in-cell) human NPC (Figure 6A) as described for the constricted conformation.[27,44] The interaction of capsid and FG-Nups was matched to experiments[17,44] (Figures S5C–S5E). To model NPC cracking, we split the scaffold and widened it (Figures 6A–6C and S7A–S7C). To mimic the larger NPC diameter in MDMs (Figure S3B), we constructed intact, dilated scaffolds (Figures S7D–S7F).

With these different NPC scaffold models, we identified the minimal steric requirements for HIV-1 capsid passage. In MD simulations of NPCs lacking the FG-Nup network (Figures S6G–S6L), steric clashes prevented passage of the capsid through the intact in-cell NPC scaffold.[27] Passage required either dilating the IR diameter to about 70 nm (Figure S6J), as seen in ~50% of MDM NPCs (Figure S3D), or cracking the NPC scaffold (Figures S6K and S6L). The additional mass of FG-Nups is expected to amplify this effect.

For a more realistic description of capsid passage, we included the FG-Nup network into our NPC models for the following simulations, as previously described.[44] In our MD simulations, FG-Nups in intact and cracked NPCs readily latched on to the HIV-1 capsid, effectively increasing the capsid diameter (Figures 6A–6C; see also Video S5). Force-driven simulations (Figures S6G–S6L) and free energy profiles for capsid passage (Figures 6D and S7) confirmed that capsid passage is possible

(C) Comparison of the median IAOP per NPC for the CR of HIV-1-infected and control MDMs. The angles are shown as boxplots and sorted by median, and angles below a threshold of 42.5° are shown in the red transparent box (purple boxes had capsids associated). Angles consistent with C8-symmetric rings are shown in the green transparent box (42.5°–47.5°). This signature was significantly more frequent in infected MDMs (see Results for details).
See also Figures S3 and S4 and Videos S3 and S4.

Please cite this article in press as: Kreysing et al., Passage of the HIV capsid cracks the nuclear pore, Cell (2025), https://doi.org/10.1016/j.cell.2024.12.008

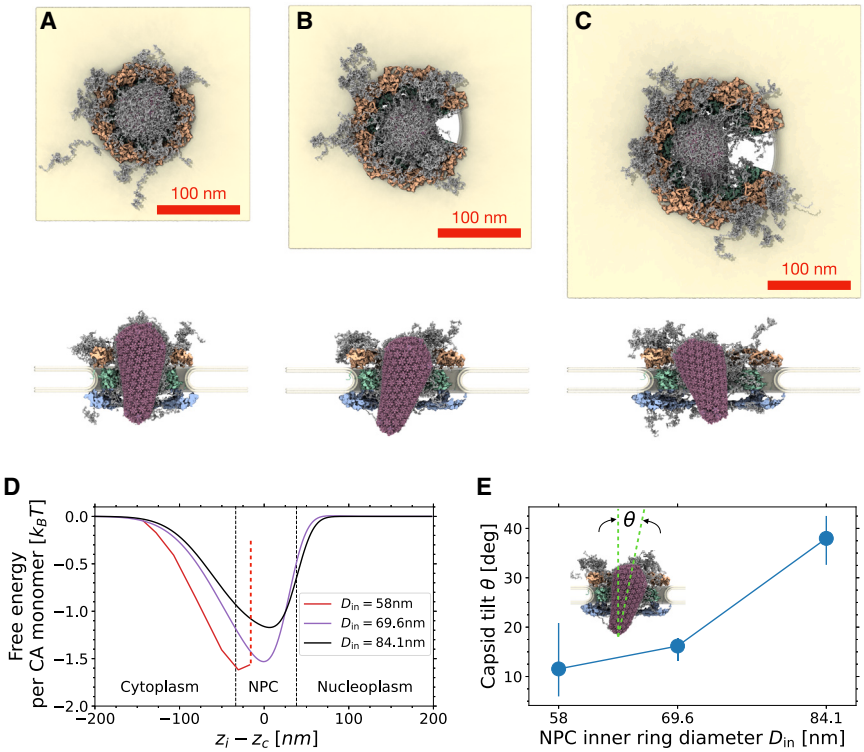

Figure 6. NPC cracking facilitates HIV-1 capsid passage

(A–C) Snapshots of MD simulations of HIV-1 capsid (pink) in intact NPC (A) with inner-ring diameter D_{in} = 58 nm and cracked NPCs with D_{in} = 69.6 nm (B) and D_{in} = 84.1 nm (C). Views from the cytosol (top) and the side (bottom) show end states of the simulations (FG-Nups: gray; CR: orange; IR: green; NR: blue; nuclear envelope: yellow).

(D) Free energy profiles for HIV-1 capsid passage through the NPC as a function of the vertical distance $z_C - z_i$ between the capsid center, halfway between its narrow and wide ends, and the inner ring (see Figures S7A–S7C for the capsid positions used to calculate the mean force shown in Figure S7D). Black dashed lines mark the extent of the NPC, and the vertical red dashed line indicates the position of the steric blockage of the HIV-1 capsid inside the intact NPC.

(E) Tilt angle (inset) of capsids released inside intact and cracked NPCs. Symbols and error bars indicate the average, minimum, and maximum at the end of three replicas. The interaction strengths $\tilde{\epsilon}_{FG-FG}$ = 0.42 and $\tilde{\epsilon}_{FG-CA}$ = 0.5 between FG-Nups and CA hexamers and pentamers were matched to experiments. The snapshots were rendered using the software VMD.[45]

See also Figures S5, S6, and S7.

in the cracked and dilated states with diameters ≥ 70 nm but sterically blocked in the ~58-nm-wide in-cell NPC. However, favorable interactions with the FG-Nups resulted in distinct free energy minima for the bound state (Figure 6D) and required further widening for the release of capsid (see Figures S6J–S6L). The favorable interactions with the FG-Nups caused the immersed capsid to tilt sideways (Figure 6E).[24]

From the MD simulations and consistent with earlier modeling,[41] we conclude that capsids face two distinct and substantial energetic barriers to exit from the central channel into the nucleus, one caused by repulsive steric interactions with the NPC and the other by the attractive interactions of the capsid with FG-Nups. As found here, the steric barrier can be relieved by NPC cracks, whereas the attractions could be broken either by capsid rupture and release of the HIV-1 genetic material into the nucleus or, alternatively, by competitive binding of additional factors such as Nup153 and CPSF6 to the CA lattice.

DISCUSSION

Based on our results, we can assess the described different scenarios for nuclear entry of HIV-1 capsids: (1) by STA we did not identify deformation of the capsid lattice within the central channel of the NPC as compared with capsids localized elsewhere. (2) We also did not observe breakage and morphological alteration of the capsid lattice inside the central channel. Instead, we obtained compelling evidence for scenario (3): passage of the HIV-1 capsid through the NPC channel altered the NPC scaffold in MDMs. Our findings support a model (Figure 7) in which capsids decorated with CypA dock to the cytoplasmic face of the NPC, where CypA is stripped off, most likely by competitive interaction with the Cyp domain of Nup358 in the CR. The capsid is then drawn into the central channel by saturating the respective FG-binding sites toward the broad end of the capsid.[32] As it penetrates more deeply, clashes with both the NPC scaffold and FG-Nups emerge. Entry into the limited space creates lateral force that in turn can lead to stretching of the NPC scaffold. NPC stretching may then extend the ring structure to a degree that it cracks, likely allowing a spatial redistribution of FG-Nups and further progression of the capsid through the NPC. We cannot exclude that capsid elasticity of scenario (1) could occur transiently and may thus contribute to nuclear entry of the capsid as well. Furthermore, potential capsid breakage, as in (2), could lead to complete capsid disintegration, thereby escaping detection. However, based on the high proportion of cracked pores and the observation of morphologically intact capsids in the nucleus, we propose that HIV-1 capsids pass the NPC more or less intact and, if sterically blocked, crack its rings.

We speculate that capsid progression toward the nucleoplasm may be driven by interactions with Nup153 FG repeats. At the nuclear basket, the capsid may transiently remain latched to the long Nup153 FG repeats and thus rotate in the chromatin-free region, as occasionally observed in the simulations. The substantial proportion of capsids at the nucleoplasmic side of NPCs further suggested that release from the nuclear basket may not be instantaneous. These observations agree with *in vitro* measurements of binding constants of different FG-Nups,[17,46] indicate delayed release into the nucleoplasm and

Please cite this article in press as: Kreysing et al., Passage of the HIV capsid cracks the nuclear pore, Cell (2025), https://doi.org/10.1016/j.cell.2024.12.008

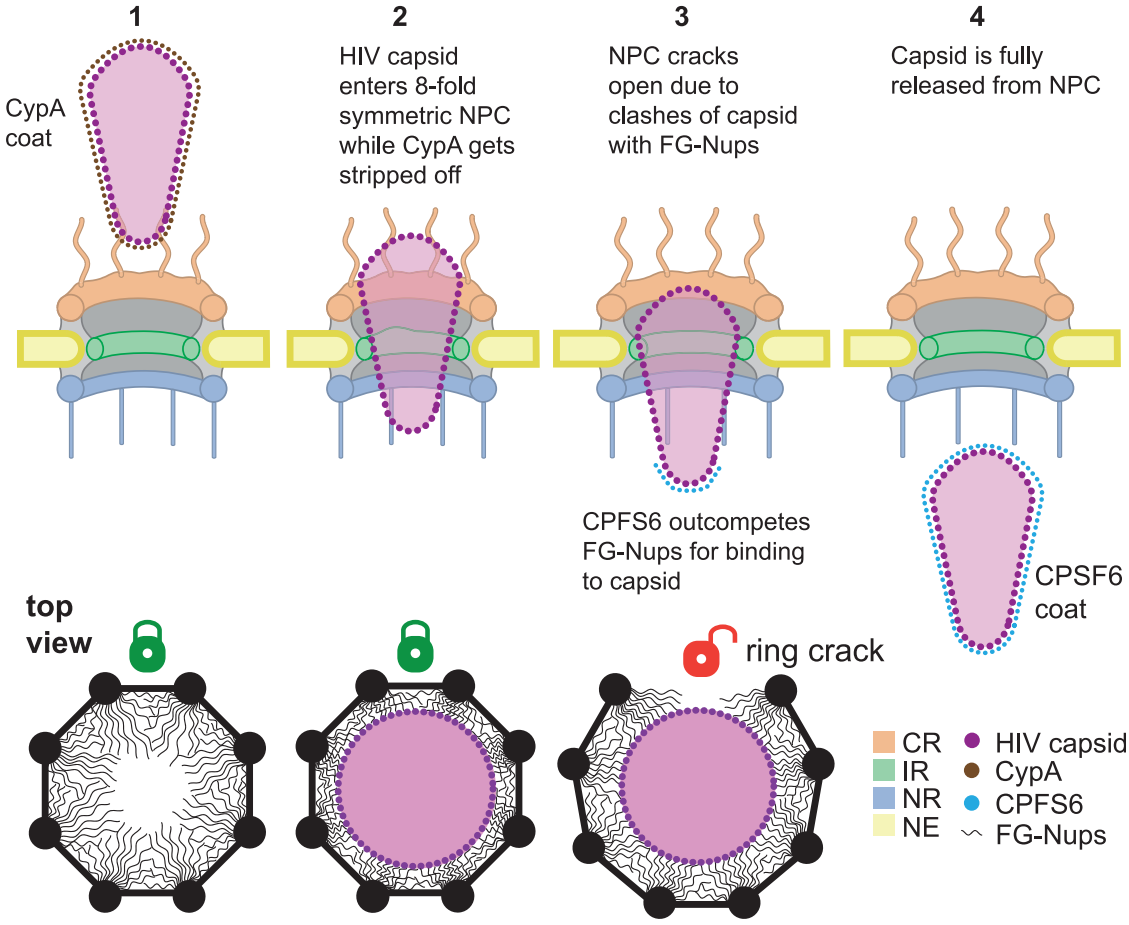

Figure 7. Model for nuclear entry of the HIV-1 capsid in macrophages

(1) Side view: a CypA-coated, cone-shaped capsid approaches the NPC guided by CR filaments. Below, the intact ring (closed lock) is shown in a top view with FG-Nups extending into the central channel. (2) The capsid partially inserts into the central channel; CypA dissociates. Its wide end has not yet passed through the narrowest constriction of the NPC scaffold. The FG-Nup meshwork is compressed. (3) The capsid cracks the NPC scaffold, fully inserting into the widened central channel. CPFS6 coats the tip of capsid that is now placed into the nucleoplasm by outcompeting FG-Nups. Within the cracked ring (open lock), the FG-Nup meshwork relaxes. (4) The capsid is released into the nucleoplasm and acquires a full CPFS6 coat. For color code, see figure.

explain the variable orientation of nuclear basket-associated capsids. Ultimately, FG-binding sites in the capsid lattice become competitively saturated by abundant nuclear CPSF6, releasing the capsid from the nuclear basket. This model is consistent with CPSF6 gene silencing experiments and mutation of the CPSF6 binding site in CA, where capsids were prominently observed close to the nuclear basket region and differences in HIV-1 integration sites were found.[20,24]

In our prior study in a T cell line,[24] we had not observed NPC cracking. However, cryo-ET had captured only a few events, and these capsids contained the A77V mutation defective in CPSF6 binding. Moreover, differences across a small set of individual particles cannot be readily detected by STA. Here, by using template matching of NPC ring subunits[42,43] we could reliably detect damage of individual NPCs and, by greatly expanding the statistics, connect NPC cracking to HIV-1 capsid passage.

That the HIV-1 capsid cracks the NPC was not necessarily intuitive. The NPC scaffold is an elaborate structure designed to persist strain laterally imposed by the nuclear membranes,[26,43,47] while the capsid has to disintegrate at some stage during the post-entry process. The exact forces remain challenging to measure experimentally. In the MD simulations, forces of 10–100 pN pull the capsid into the NPC central channel (Figure S7D), which is in the range of forces required for sub-second unfolding of proteins.[48] The cone shape of stuck capsids converts this axial force into a radial force that could drive NPC cracking. Instead of the NPC cracking the capsid, the capsid cracks the NPC.

Our findings provide a potential explanation for the evolution of the unique HIV-1 capsid structure. Genome protection and reverse transcription inside a protective shell requires a closed structure, but not this cone-shaped geometry. However, the complete capsid also acts as the importin for nuclear entry of the HIV-1 subviral complex,[33,34] and this is absolutely essential for infection of postmitotic cells. Shape most likely reflects function: the narrow end facilitates threading into the narrow channel of the NPC, and the increasing width of the cone accommodates the volume requirement for the genome and provides avidity effects by an increasing number of FG-binding sites as the capsid

progresses into the NPC. Maximum width may be a trade-off between what is needed to package the genome (most likely together with partial cDNA due to cytoplasmic reverse transcription) and the size limit to pass through the (partly disintegrated) NPC channel. NPC cracking may thus be a byproduct of HIV-1 nuclear entry with optimal payload, without any direct consequences for infectivity. Importantly, damage to individual NPCs must be compatible with cell viability, as infected macrophages can survive for prolonged time, and we found no evidence for rupture of the NE. Could there be a further benefit from NPC cracking for the virus? One may speculate that the capsid lattice becomes mechanically prepared for rupture while it sheers at the NPC scaffold but does not immediately disintegrate because of rapid surface coating with CPSF6 upon reaching the nuclear side.

Limitations of the study

Our study is limited by the fact that the number of events observed by cryo-ET is relatively small and the technique is not time resolved. Thus, cracking cannot be observed as a process. However, previous *in vitro* studies have established that the HIV-1 capsid interacts with FG-Nups,[33,34] and it is therefore plausible that it approaches an energy minimum when moving toward the central channel. Further, there is no formal proof that the observed capsids had the potential to give rise to infection. We frequently observed morphologically intact nuclear capsids in MDMs, and their size was comparable to those in virions, and NPC cracking was also observed with capsids post NPC, however, arguing against off-pathway aggregation at NPCs. At last, the resolution of STA was not sufficient to identify the secondary structure of CypA, but there is ample evidence in the literature that cytoplasmic HIV-1 capsids are decorated with CypA,[10,11,23,49] and the respective binding site was clearly occupied in our data.

RESOURCE AVAILABILITY

Lead contact

Further information and requests for resources and reagents should be directed to and will be fulfilled by the lead contact, Martin Beck (martin.beck@biophys.mpg.de).

Materials availability

All unique/stable reagents generated in this study are available from the lead contact with a completed material transfer agreement.

Data and code availability

- Cryo-ET STA HIV-1 capsid hexamer and pentamer maps reported in this paper are deposited in the EMDB with the accession codes listed in the key resources table. The NPC maps are also deposited in the EMDB with the accession codes listed in the key resources table.
- The raw tilt series, the cleaned and dose-filtered tilt series, the alignment files, and the reconstructed tomograms for both NNHIV- and mock-infected conditions are deposited with accession codes EMPIAR: 12454 and EMPIAR: 12457, respectively.
- Initial configurations and trajectories of the MD simulations, including the respective structural models, are available under CC-BY license under Zenodo: https://doi.org/10.5281/zenodo.14179289.
- Code is made available at https://github.com/turonova/cryoCAT and archived under Zenodo: https://doi.org/10.5281/zenodo.13916774.[50]
- Any additional information required to reanalyze the data reported in this paper is available from the lead contact upon request.

ACKNOWLEDGMENTS

We thank all members of the Beck, Hummer, and Kräusslich laboratories for helpful discussions. We thank Erica Margiotta for discussions and scientific training. We are grateful to Mark Linder and the members of the Central Electron Microscopy facility of the Max Planck Institute of Biophysics for technical support and support with data acquisition. We also thank the Infectious Diseases Imaging Platform (IDIP) at the Center for Integrative Infectious Disease Research and the Electron Microscopy Core Facility of Heidelberg University. We are grateful to Maria Anders-Össwein, Anke-Mareil Heuser, Vera Sonntag-Buck, and Severina Klaus for MDM preparation and experimental support. We thank Özkan Yildiz, Juan F. Castillo Hernandez, Thomas Hoffmann, and Andre Schwarz for discussions and the Max Planck Computing and Data Facility for support with scientific computing. We are grateful to Stefanie Böhm and Barbara Müller for careful reading and advice during manuscript preparation. J.P.K. thanks the International Max Planck Research School (IMPRS) on Cellular Biophysics. Funding is as follows: this work was supported by the Deutsche Forschungsgemeinschaft (DFG, German Research Foundation) Projektnummer 240245660-SFB 1129, project 5 (H.-G.K.) and project 20 (M.B.), and Projektnummer 450648163-SFB 1507, project 12 (G.H.). G.H. and M.B. acknowledge funding by the Max Planck Society and by the Chan Zuckerberg Initiative.

AUTHOR CONTRIBUTIONS

J.P.K., V.Z., G.H., H.-G.K., and M.B. conceived the project. V.Z. and L.R. designed and performed the fluorescence microscopy and CLEM experiments with help from V.L. and analyzed data. J.P.K. performed the cryo-ET data acquisition with help from S.W. and V.Z. J.P.K. performed STA, template matching, and subsequent data analysis with help from B.T. M.H. performed the MD simulations with help from S.C.-L. The manuscript was written by J.P.K., M.H., V.Z., G.H., H.-G.K., and M.B. A.O.-K. and J.K. provided important contributions to NPC structure analysis and statistical analysis, respectively. All authors contributed to manuscript editing and approved the final manuscript.

DECLARATION OF INTERESTS

M.B. is a member of the editorial board of *Cell*.

STAR★METHODS

Detailed methods are provided in the online version of this paper and include the following:

- KEY RESOURCES TABLE
- EXPERIMENTAL MODEL AND STUDY PARTICIPANT DETAILS
- METHOD DETAILS
  - Plasmids
  - Antibodies
  - Virus and virus-like particles
  - Sample preparation for confocal and STED microscopy
  - Spinning disc confocal microscopy
  - STED microscopy
  - Image analysis
  - Sample preparation for CLEM
  - CLEM and electron tomography
  - Quantitative image analysis of capsids acquired by CLEM-ET
  - MDM vitrification and cryo-FIB milling
  - MDM cryo-ET data acquisition
  - Tomogram reconstruction
  - HIV CA hexamer subtomogram averaging
  - HIV CA pentamer subtomogram averaging
  - HIV CA pentamer template matching
  - NPC particle selection and subtomogram averaging
  - NPC diameter measurements
  - NPC ring subunit template matching
  - NPC ring subunit interior angle of polygon (IAOP) measurements

- In-situ capsid modeling
- Coarse-grained model of NPC and HIV capsid
- Labelling the outer surface particles of HIV capsid
- Binding affinity of a strand of FG-Nup153 to CA hexamers
- Modelling cracks in NPC scaffold
- Force-driven passage of HIV capsid through NPC
- Free energy profile for HIV capsid passage through NPC
- Release and tilt of HIV capsid inside NPC

- QUANTIFICATION AND STATISTICAL ANALYSIS

SUPPLEMENTAL INFORMATION

Supplemental information can be found online at https://doi.org/10.1016/j.cell.2024.12.008.

Received: April 23, 2024
Revised: November 12, 2024
Accepted: December 9, 2024
Published: January 17, 2025

REFERENCES

1. Yamashita, M., and Emerman, M. (2006). Retroviral infection of non-dividing cells: old and new perspectives. Virology *344*, 88–93. https://doi.org/10.1016/j.virol.2005.09.012.
2. Ananth, S., Ambiel, I., Schifferdecker, S., Müller, T.G., Wratil, P.R., Mejias-Perez, E., Kräusslich, H.G., Müller, B., Keppler, O.T., and Fackler, O.T. (2024). Spatial resolution of HIV-1 post-entry steps in resting CD4 T cells. Cell Rep. *43*, 113941. https://doi.org/10.1016/j.celrep.2024.113941.
3. Dharan, A., Bachmann, N., Talley, S., Zwikelmaier, V., and Campbell, E.M. (2020). Nuclear pore blockade reveals that HIV-1 completes reverse transcription and uncoating in the nucleus. Nat. Microbiol. *5*, 1088–1095. https://doi.org/10.1038/s41564-020-0735-8.
4. Müller, T.G., Zila, V., Peters, K., Schifferdecker, S., Stanic, M., Lucic, B., Laketa, V., Lusic, M., Müller, B., and Kräusslich, H.G. (2021). HIV-1 uncoating by release of viral cDNA from capsid-like structures in the nucleus of infected cells. eLife *10*, e64776. https://doi.org/10.7554/eLife.64776.
5. Jang, S., and Engelman, A.N. (2023). Capsid–host interactions for HIV-1 ingress. Microbiol. Mol. Biol. Rev. *87*, e0004822. https://doi.org/10.1128/mmbr.00048-22.
6. Müller, T.G., Zila, V., Müller, B., and Kräusslich, H.G. (2022). Nuclear capsid uncoating and reverse transcription of HIV-1. Annu. Rev. Virol. *9*, 261–284. https://doi.org/10.1146/annurev-virology-020922-110929.
7. McDonald, D., Vodicka, M.A., Lucero, G., Svitkina, T.M., Borisy, G.G., Emerman, M., and Hope, T.J. (2002). Visualization of the intracellular behavior of HIV in living cells. J. Cell Biol. *159*, 441–452. https://doi.org/10.1083/jcb.200203150.
8. Badieyan, S., Lichon, D., Andreas, M.P., Gillies, J.P., Peng, W., Shi, J., DeSantis, M.E., Aiken, C.R., Böcking, T., Giessen, T.W., et al. (2023). HIV-1 binds dynein directly to hijack microtubule transport machinery. Preprint at bioRxiv. https://doi.org/10.1101/2023.08.29.555335.
9. Naghavi, M.H. (2021). HIV-1 capsid exploitation of the host microtubule cytoskeleton during early infection. Retrovirology *18*, 19. https://doi.org/10.1186/s12977-021-00563-3.
10. Luban, J., Bossolt, K.L., Franke, E.K., Kalpana, G.V., and Goff, S.P. (1993). Human immunodeficiency virus type 1 Gag protein binds to cyclophilins A and B. Cell *73*, 1067–1078. https://doi.org/10.1016/0092-8674(93)90637-6.
11. Gamble, T.R., Vajdos, F.F., Yoo, S., Worthylake, D.K., Houseweart, M., Sundquist, W.I., and Hill, C.P. (1996). Crystal structure of human cyclophilin A bound to the amino-terminal domain of HIV-1 capsid. Cell *87*, 1285–1294. https://doi.org/10.1016/s0092-8674(00)81823-1.
12. Dharan, A., Talley, S., Tripathi, A., Mamede, J.I., Majetschak, M., Hope, T.J., and Campbell, E.M. (2016). KIF5B and Nup358 cooperatively mediate the nuclear import of HIV-1 during infection. PLoS Pathog. *12*, e1005700. https://doi.org/10.1371/journal.ppat.1005700.
13. Ganser, B.K., Li, S., Klishko, V.Y., Finch, J.T., and Sundquist, W.I. (1999). Assembly and analysis of conical models for the HIV-1 core. Science *283*, 80–83. https://doi.org/10.1126/science.283.5398.80.
14. Zhao, G., Perilla, J.R., Yufenyuy, E.L., Meng, X., Chen, B., Ning, J., Ahn, J., Gronenborn, A.M., Schulten, K., Aiken, C., et al. (2013). Mature HIV-1 capsid structure by cryo-electron microscopy and all-atom molecular dynamics. Nature *497*, 643–646. https://doi.org/10.1038/nature12162.
15. Mattei, S., Glass, B., Hagen, W.J.H., Kräusslich, H.-G., and Briggs, J.A.G. (2016). The structure and flexibility of conical HIV-1 capsids determined within intact virions. Science *354*, 1434–1437. https://doi.org/10.1126/science.aah4972.
16. Matreyek, K.A., Yücel, S.S., Li, X., and Engelman, A. (2013). Nucleoporin NUP153 phenylalanine-glycine motifs engage a common binding pocket within the HIV-1 capsid protein to mediate lentiviral infectivity. PLoS Pathog. *9*, e1003693. https://doi.org/10.1371/journal.ppat.1003693.
17. Price, A.J., Jacques, D.A., McEwan, W.A., Fletcher, A.J., Essig, S., Chin, J.W., Halambage, U.D., Aiken, C., and James, L.C. (2014). Host cofactors and pharmacologic ligands share an essential interface in HIV-1 capsid that is lost upon disassembly. PLoS Pathog. *10*, e1004459. https://doi.org/10.1371/journal.ppat.1004459.
18. Yant, S.R., Mulato, A., Hansen, D., Tse, W.C., Niedziela-Majka, A., Zhang, J.R., Stepan, G.J., Jin, D., Wong, M.H., Perreira, J.M., et al. (2019). A highly potent long-acting small-molecule HIV-1 capsid inhibitor with efficacy in a humanized mouse model. Nat. Med. *25*, 1377–1384. https://doi.org/10.1038/s41591-019-0560-x.
19. Bester, S.M., Wei, G., Zhao, H., Adu-Ampratwum, D., Iqbal, N., Courouble, V.V., Francis, A.C., Annamalai, A.S., Singh, P.K., Shkriabai, N., et al. (2020). Structural and mechanistic bases for a potent HIV-1 capsid inhibitor. Science *370*, 360–364. https://doi.org/10.1126/science.abb4808.
20. Bejarano, D.A., Peng, K., Laketa, V., Börner, K., Jost, K.L., Lucic, B., Glass, B., Lusic, M., Müller, B., and Kräusslich, H.G. (2019). HIV-1 nuclear import in macrophages is regulated by CPSF6-capsid interactions at the nuclear pore complex. eLife *8*, e41800. https://doi.org/10.7554/eLife.41800.
21. von Appen, A., Kosinski, J., Sparks, L., Ori, A., DiGuilio, A.L., Vollmer, B., Mackmull, M.T., Banterle, N., Parca, L., Kastritis, P., et al. (2015). In situ structural analysis of the human nuclear pore complex. Nature *526*, 140–143. https://doi.org/10.1038/nature15381.
22. Mallery, D.L., Márquez, C.L., McEwan, W.A., Dickson, C.F., Jacques, D.A., Anandapadamanaban, M., Bichel, K., Towers, G.J., Saiardi, A., Böcking, T., et al. (2018). IP6 is an HIV pocket factor that prevents capsid collapse and promotes DNA synthesis. eLife *7*, e35335. https://doi.org/10.7554/eLife.35335.
23. Francis, A.C., and Melikyan, G.B. (2018). Single HIV-1 imaging reveals progression of infection through CA-dependent steps of docking at the nuclear pore, uncoating, and nuclear transport. Cell Host Microbe *23*, 536–548.e6. https://doi.org/10.1016/j.chom.2018.03.009.
24. Zila, V., Margiotta, E., Turoňová, B., Müller, T.G., Zimmerli, C.E., Mattei, S., Allegretti, M., Börner, K., Rada, J., Müller, B., et al. (2021). Cone-shaped HIV-1 capsids are transported through intact nuclear pores. Cell *184*, 1032–1046.e18. https://doi.org/10.1016/j.cell.2021.01.025.
25. Schifferdecker, S., Zila, V., Müller, T.G., Sakin, V., Anders-Össwein, M., Laketa, V., Kräusslich, H.G., and Müller, B. (2022). Direct capsid labeling of infectious HIV-1 by genetic code expansion allows detection of largely complete nuclear capsids and suggests nuclear entry of HIV-1 complexes via common routes. mBio *13*, e0195922. https://doi.org/10.1128/mbio.01959-22.
26. Zimmerli, C.E., Allegretti, M., Rantos, V., Goetz, S.K., Obarska-Kosinska, A., Zagoriy, I., Halavatyi, A., Hummer, G., Mahamid, J., Kosinski, J., et al. (2021). Nuclear pores dilate and constrict in cellulo. Science *374*, eabd9776. https://doi.org/10.1126/science.abd9776.

27. Mosalaganti, S., Obarska-Kosinska, A., Siggel, M., Taniguchi, R., Turoňová, B., Zimmerli, C.E., Buczak, K., Schmidt, F.H., Margiotta, E., Mackmull, M.T., et al. (2022). AI-based structure prediction empowers integrative structural analysis of human nuclear pores. Science *376*, eabm9506. https://doi.org/10.1126/science.abm9506.

28. Mahamid, J., Pfeffer, S., Schaffer, M., Villa, E., Danev, R., Cuellar, L.K., Förster, F., Hyman, A.A., Plitzko, J.M., and Baumeister, W. (2016). Visualizing the molecular sociology at the HeLa cell nuclear periphery. Science *351*, 969–972. https://doi.org/10.1126/science.aad8857.

29. Schuller, A.P., Wojtynek, M., Mankus, D., Tatli, M., Kronenberg-Tenga, R., Regmi, S.G., Dip, P.V., Lytton-Jean, A.K.R., Brignole, E.J., Dasso, M., et al. (2021). The cellular environment shapes the nuclear pore complex architecture. Nature *598*, 667–671. https://doi.org/10.1038/s41586-021-03985-3.

30. Petrovic, S., Samanta, D., Perriches, T., Bley, C.J., Thierbach, K., Brown, B., Nie, S., Mobbs, G.W., Stevens, T.A., Liu, X., et al. (2022). Architecture of the linker-scaffold in the nuclear pore. Science *376*, eabm9798. https://doi.org/10.1126/science.abm9798.

31. Görlich, D., and Kutay, U. (1999). Transport between the cell nucleus and the cytoplasm. Annu. Rev. Cell Dev. Biol. *15*, 607–660. https://doi.org/10.1146/annurev.cellbio.15.1.607.

32. Shen, Q., Feng, Q., Wu, C., Xiong, Q., Tian, T., Yuan, S., Shi, J., Bedwell, G.J., Yang, R., Aiken, C., et al. (2023). Modeling HIV-1 nuclear entry with nucleoporin-gated DNA-origami channels. Nat. Struct. Mol. Biol. *30*, 425–435. https://doi.org/10.1038/s41594-023-00925-9.

33. Fu, L., Weiskopf, E.N., Akkermans, O., Swanson, N.A., Cheng, S., Schwartz, T.U., and Görlich, D. (2024). HIV-1 capsids enter the FG phase of nuclear pores like a transport receptor. Nature *626*, 843–851. https://doi.org/10.1038/s41586-023-06966-w.

34. Dickson, C.F., Hertel, S., Tuckwell, A.J., Li, N., Ruan, J., Al-Izzi, S.C., Ariotti, N., Sierecki, E., Gambin, Y., Morris, R.G., et al. (2024). The HIV capsid mimics karyopherin engagement of FG-nucleoporins. Nature *626*, 836–842. https://doi.org/10.1038/s41586-023-06969-7.

35. Deshpande, A., Bryer, A.J., Andino-Moncada, J.R., Shi, J., Hong, J., Torres, C., Harel, S., Francis, A.C., Perilla, J.R., Aiken, C., et al. (2024). Elasticity of the HIV-1 core facilitates nuclear entry and infection. PLoS Pathog. *20*, e1012537. https://doi.org/10.1371/journal.ppat.1012537.

36. Bejarano, D.A., Puertas, M.C., Börner, K., Martinez-Picado, J., Müller, B., and Kräusslich, H.G. (2018). Detailed characterization of early HIV-1 replication dynamics in primary human macrophages. Viruses *10*, 620. https://doi.org/10.3390/v10110620.

37. Thevathasan, J.V., Kahnwald, M., Cieśliński, K., Hoess, P., Peneti, S.K., Reitberger, M., Heid, D., Kasuba, K.C., Hoerner, S.J., Li, Y., et al. (2019). Nuclear pores as versatile reference standards for quantitative superresolution microscopy. Nat. Methods *16*, 1045–1053. https://doi.org/10.1038/s41592-019-0574-9.

38. Briggs, J.A.G., Wilk, T., Welker, R., Kräusslich, H.G., and Fuller, S.D. (2003). Structural organization of authentic, mature HIV-1 virions and cores. EMBO J. *22*, 1707–1715. https://doi.org/10.1093/emboj/cdg143.

39. Ni, T., Zhu, Y., Yang, Z., Xu, C., Chaban, Y., Nesterova, T., Ning, J., Böcking, T., Parker, M.W., Monnie, C., et al. (2021). Structure of native HIV-1 cores and their interactions with IP6 and CypA. Sci. Adv. *7*, eabj5715. https://doi.org/10.1126/sciadv.abj5715.

40. Briggs, J.A.G., Grünewald, K., Glass, B., Förster, F., Kräusslich, H.G., and Fuller, S.D. (2006). The mechanism of HIV-1 core assembly: insights from three-dimensional reconstructions of authentic virions. Structure *14*, 15–20. https://doi.org/10.1016/j.str.2005.09.010.

41. Hudait, A., and Voth, G.A. (2024). HIV-1 capsid shape, orientation, and entropic elasticity regulate translocation into the nuclear pore complex. Proc. Natl. Acad. Sci. USA *121*, e2313737121. https://doi.org/10.1073/pnas.2313737121.

42. Cruz-León, S., Majtner, T., Hoffmann, P.C., Kreysing, J.P., Kehl, S., Tuijtel, M.W., Schaefer, S.L., Geißler, K., Beck, M., Turoňová, B., et al. (2024). High-confidence 3D template matching for cryo-electron tomography. Nat. Commun. *15*, 3992. https://doi.org/10.1038/s41467-024-47839-8.

43. Taniguchi, R., Orniacki, C., Kreysing, J.P., Zila, V., Zimmerli, C.E., Böhm, S., Turoňová, B., Kräusslich, H.-G., Doye, V., and Beck, M. (2024). Nuclear pores safeguard the integrity of the nuclear envelope. Preprint at bioRxiv. https://doi.org/10.1101/2024.02.05.578890.

44. Yu, M., Heidari, M., Mikhaleva, S., Tan, P.S., Mingu, S., Ruan, H., Reinkemeier, C.D., Obarska-Kosinska, A., Siggel, M., Beck, M., et al. (2023). Visualizing the disordered nuclear transport machinery in situ. Nature *617*, 162–169. https://doi.org/10.1038/s41586-023-05990-0.

45. Humphrey, W., Dalke, A., and Schulten, K. (1996). VMD: visual molecular dynamics. J. Mol. Graph. *14*, 33–38. https://doi.org/10.1016/0263-7855(96)00018-5.

46. Bhattacharya, A., Alam, S.L., Fricke, T., Zadrozny, K., Sedzicki, J., Taylor, A.B., Demeler, B., Pornillos, O., Ganser-Pornillos, B.K., Diaz-Griffero, F., et al. (2014). Structural basis of HIV-1 capsid recognition by PF74 and CPSF6. Proc. Natl. Acad. Sci. USA *111*, 18625–18630. https://doi.org/10.1073/pnas.1419945112.

47. Hoffmann, P.C., Kim, H., Obarska-Kosinska, A., Kreysing, J.P., Andino-Frydman, E., Cruz-León, S., Margiotta, E., Cernikova, L., Kosinski, J., Turoňová, B., et al. (2024). Nuclear pore permeability and fluid floware modulated by its dilation state. Mol. Cell, 85. https://doi.org/10.1016/j.molcel.2024.11.038.

48. Zoldák, G., and Rief, M. (2013). Force as a single molecule probe of multidimensional protein energy landscapes. Curr. Opin. Struct. Biol. *23*, 48–57. https://doi.org/10.1016/j.sbi.2012.11.007.

49. Liu, C., Perilla, J.R., Ning, J., Lu, M., Hou, G., Ramalho, R., Himes, B.A., Zhao, G., Bedwell, G.J., Byeon, I.J., et al. (2016). Cyclophilin A stabilizes the HIV-1 capsid through a novel non-canonical binding site. Nat. Commun. *7*, 10714. https://doi.org/10.1038/ncomms10714.

50. Turoňová, B. (2024). cryoCAT [software]. 10.5281/zenodo.13916774.

51. Welker, R., Hohenberg, H., Tessmer, U., Huckhagel, C., and Kräusslich, H.G. (2000). Biochemical and structural analysis of isolated mature cores of human immunodeficiency virus type 1. J. Virol. *74*, 1168–1177. https://doi.org/10.1128/jvi.74.3.1168-1177.2000.

52. Pear, W.S., Nolan, G.P., Scott, M.L., and Baltimore, D. (1993). Production of high-titer helper-free retroviruses by transient transfection. Proc. Natl. Acad. Sci. USA *90*, 8392–8396. https://doi.org/10.1073/pnas.90.18.8392.

53. Schnell, G., Joseph, S., Spudich, S., Price, R.W., and Swanstrom, R. (2011). HIV-1 replication in the central nervous system occurs in two distinct cell types. PLoS Pathog. *7*, e1002286. https://doi.org/10.1371/journal.ppat.1002286.

54. Albanese, A., Arosio, D., Terreni, M., and Cereseto, A. (2008). HIV-1 preintegration complexes selectively target decondensed chromatin in the nuclear periphery. PLoS One *3*, e2413. https://doi.org/10.1371/journal.pone.0002413.

55. Schindelin, J., Arganda-Carreras, I., Frise, E., Kaynig, V., Longair, M., Pietzsch, T., Preibisch, S., Rueden, C., Saalfeld, S., Schmid, B., et al. (2012). Fiji: an open-source platform for biological-image analysis. Nat. Methods *9*, 676–682. https://doi.org/10.1038/nmeth.2019.

56. Mastronarde, D.N. (2005). Automated electron microscope tomography using robust prediction of specimen movements. J. Struct. Biol. *152*, 36–51. https://doi.org/10.1016/j.jsb.2005.07.007.

57. Kremer, J.R., Mastronarde, D.N., and McIntosh, J.R. (1996). Computer visualization of three-dimensional image data using IMOD. J. Struct. Biol. *116*, 71–76. https://doi.org/10.1006/jsbi.1996.0013.

58. de Chaumont, F., Dallongeville, S., Chenouard, N., Hervé, N., Pop, S., Provoost, T., Meas-Yedid, V., Pankajakshan, P., Lecomte, T., Le Montagner, Y., et al. (2012). Icy: an open BioImage informatics platform for extended reproducible research. Nat. Methods *9*, 690–696. https://doi.org/10.1038/nmeth.2075.

59. Paul-Gilloteaux, P., Heiligenstein, X., Belle, M., Domart, M.C., Larijani, B., Collinson, L., Raposo, G., and Salamero, J. (2017). eC-CLEM: flexible

multidimensional registration software for correlative microscopies. Nat. Methods *14*, 102–103. https://doi.org/10.1038/nmeth.4170.

60. napari contributors (2024). napari: a multi-dimensional image viewer for Python [software]. 10.5281/zenodo.13859720.
61. Goddard, T.D., Huang, C.C., Meng, E.C., Pettersen, E.F., Couch, G.S., Morris, J.H., and Ferrin, T.E. (2018). UCSF ChimeraX: meeting modern challenges in visualization and analysis. Protein Sci. *27*, 14–25. https://doi.org/10.1002/pro.3235.
62. Ermel, U.H., Arghittu, S.M., and Frangakis, A.S. (2022). ArtiaX: an electron tomography toolbox for the interactive handling of sub-tomograms in UCSF ChimeraX. Protein Sci. *31*, e4472. https://doi.org/10.1002/pro.4472.
63. Zivanov, J., Nakane, T., Forsberg, B.O., Kimanius, D., Hagen, W.J., Lindahl, E., and Scheres, S.H. (2018). New tools for automated high-resolution cryo-EM structure determination in RELION-3. eLife *7*, e42166. https://doi.org/10.7554/eLife.42166.
64. Turoňová, B., Schur, F.K.M., Wan, W., and Briggs, J.A.G. (2017). Efficient 3D-CTF correction for cryo-electron tomography using NovaCTF improves subtomogram averaging resolution to 3.4Å. J. Struct. Biol. *199*, 187–195. https://doi.org/10.1016/j.jsb.2017.07.007.
65. Turoňová, B. (2020). Fourier3D [software]. 10.5281/zenodo.3973621.
66. Turoňová, B. (2022). novaSTA [software]. 10.5281/zenodo.5921012.
67. Zheng, S., Wolff, G., Greenan, G., Chen, Z., Faas, F.G.A., Bárcena, M., Koster, A.J., Cheng, Y., and Agard, D.A. (2022). AreTomo: an integrated software package for automated marker-free, motion-corrected cryo-electron tomographic alignment and reconstruction. J. Struct. Biol. X *6*, 100068. https://doi.org/10.1016/j.yjsbx.2022.100068.
68. Turoňová, B. (2024). GAPStop(TM) – GPU Accelerated Python-Base Stopgap for Template Matching [software]. 10.5281/zenodo.10822455.
69. Waterhouse, A., Bertoni, M., Bienert, S., Studer, G., Tauriello, G., Gumienny, R., Heer, F.T., de Beer, T.A.P., Rempfer, C., Bordoli, L., et al. (2018). SWISS-MODEL: homology modelling of protein structures and complexes. Nucleic Acids Res. *46*, W296–W303. https://doi.org/10.1093/nar/gky427.
70. Plimpton, S. (1995). Fast parallel algorithms for short-range Molecular Dynamics. J. Comp. Phys. *117*, 1–19. https://doi.org/10.1006/jcph.1995.1039.
71. Abraham, M.J., Murtola, T., Schulz, R., Páll, S., Smith, J.C., Hess, B., and Lindahl, E. (2015). GROMACS: high performance molecular simulations through multi-level parallelism from laptops to supercomputers. SoftwareX *1–2*, 19–25. https://doi.org/10.1016/j.softx.2015.06.001.
72. Adachi, A., Gendelman, H.E., Koenig, S., Folks, T., Willey, R., Rabson, A., and Martin, M.A. (1986). Production of acquired immunodeficiency syndrome-associated retrovirus in human and nonhuman cells transfected with an infectious molecular clone. J. Virol. *59*, 284–291. https://doi.org/10.1128/JVI.59.2.284-291.1986.
73. Pizzato, M., Erlwein, O., Bonsall, D., Kaye, S., Muir, D., and McClure, M.O. (2009). A one-step SYBR Green I-based product-enhanced reverse transcriptase assay for the quantitation of retroviruses in cell culture supernatants. J. Virol. Methods *156*, 1–7. https://doi.org/10.1016/j.jviromet.2008.10.012.
74. Staudt, T., Engler, A., Rittweger, E., Harke, B., Engelhardt, J., and Hell, S.W. (2011). Far-field optical nanoscopy with reduced number of state transition cycles. Opt. Express *19*, 5644–5657. https://doi.org/10.1364/OE.19.005644.
75. Kukulski, W., Schorb, M., Welsch, S., Picco, A., Kaksonen, M., and Briggs, J.A.G. (2011). Correlated fluorescence and 3D electron microscopy with high sensitivity and spatial precision. J. Cell Biol. *192*, 111–119. https://doi.org/10.1083/jcb.201009037.
76. Schorb, M., Gaechter, L., Avinoam, O., Sieckmann, F., Clarke, M., Bebeacua, C., Bykov, Y.S., Sonnen, A.F.P., Lihl, R., and Briggs, J.A.G. (2017). New hardware and workflows for semi-automated correlative cryo-fluorescence and cryo-electron microscopy/tomography. J. Struct. Biol. *197*, 83–93. https://doi.org/10.1016/j.jsb.2016.06.020.
77. Schaffer, M., Engel, B.D., Laugks, T., Mahamid, J., Plitzko, J.M., and Baumeister, W. (2015). Cryo-focused ion beam sample preparation for imaging vitreous cells by cryo-electron tomography. Bio Protoc. *5*, e1575. https://doi.org/10.21769/bioprotoc.1575.
78. Hagen, W.J.H., Wan, W., and Briggs, J.A.G. (2017). Implementation of a cryo-electron tomography tilt-scheme optimized for high resolution subtomogram averaging. J. Struct. Biol. *197*, 191–198. https://doi.org/10.1016/j.jsb.2016.06.007.
79. Grant, T., and Grigorieff, N. (2015). Measuring the optimal exposure for single particle cryo-EM using a 2.6 Å reconstruction of rotavirus VP6. eLife *4*, e06980. https://doi.org/10.7554/eLife.06980.
80. Wan, W., Kolesnikova, L., Clarke, M., Koehler, A., Noda, T., Becker, S., and Briggs, J.A.G. (2017). Structure and assembly of the Ebola virus nucleocapsid. Nature *551*, 394–397. https://doi.org/10.1038/nature24490.
81. Allegretti, M., Zimmerli, C.E., Rantos, V., Wilfling, F., Ronchi, P., Fung, H.K.H., Lee, C.W., Hagen, W., Turoňová, B., Karius, K., et al. (2020). In-cell architecture of the nuclear pore and snapshots of its turnover. Nature *586*, 796–800. https://doi.org/10.1038/s41586-020-2670-5.
82. Wan, W., Khavnekar, S., and Wagner, J. (2024). STOPGAP: an open-source package for template matching, subtomogram alignment and classification. Acta Crystallogr. D Struct. Biol. *80*, 336–349. https://doi.org/10.1107/S205979832400295X.
83. Stacey, J.C.V., Tan, A., Lu, J.M., James, L.C., Dick, R.A., and Briggs, J.A.G. (2023). Two structural switches in HIV-1 capsid regulate capsid curvature and host factor binding. Proc. Natl. Acad. Sci. USA *120*, e2220557120. https://doi.org/10.1073/pnas.2220557120.
84. Highland, C.M., Tan, A., Ricaña, C.L., Briggs, J.A.G., and Dick, R.A. (2023). Structural insights into HIV-1 polyanion-dependent capsid lattice formation revealed by single particle cryo-EM. Proc. Natl. Acad. Sci. USA *120*, e2220545120. https://doi.org/10.1073/pnas.2220545120.
85. Jorgensen, W.L., Chandrasekhar, J., Madura, J.D., Impey, R.W., and Klein, M.L. (1983). Comparison of simple potential functions for simulating liquid water. J. Chem. Phys. *79*, 926–935. https://doi.org/10.1063/1.445869.
86. Lindorff-Larsen, K., Piana, S., Palmo, K., Maragakis, P., Klepeis, J.L., Dror, R.O., and Shaw, D.E. (2010). Improved side-chain torsion potentials for the Amber ff99SB protein force field. Proteins *78*, 1950–1958. https://doi.org/10.1002/prot.22711.
87. Mamatkulov, S., and Schwierz, N. (2018). Force fields for monovalent and divalent metal cations in TIP3P water based on thermodynamic and kinetic properties. J. Chem. Phys. *148*, 74504. https://doi.org/10.1063/1.5017694.
88. Essmann, U., Perera, L., Berkowitz, M.L., Darden, T., Lee, H., and Pedersen, L.G. (1995). A smooth particle mesh Ewald method. J. Chem. Phys. *103*, 8577–8593. https://doi.org/10.1063/1.470117.
89. Parrinello, M., and Rahman, A. (1981). Polymorphic transitions in single crystals: A new molecular dynamics method. J. Appl. Phys. *52*, 7182–7190. https://doi.org/10.1063/1.328693.
90. Bussi, G., Donadio, D., and Parrinello, M. (2007). Canonical sampling through velocity rescaling. J. Chem. Phys. *126*, 014101. https://doi.org/10.1063/1.2408420.
91. Kremer, K., and Grest, G.S. (1990). Dynamics of entangled linear polymer melts: A molecular-dynamics simulation. J. Chem. Phys. *92*, 5057–5086. https://doi.org/10.1063/1.458541.
92. Boyd, K.J., and May, E.R. (2018). BUMPy: A model-independent tool for constructing lipid bilayers of varying curvature and composition. J. Chem. Theor. Comput. *14*, 6642–6652. https://doi.org/10.1021/acs.jctc.8b00765.
93. Dünweg, B., and Paul, W. (1991). Brownian dynamics simulations without Gaussian random numbers. Int. J. Mod. Phys. C *02*, 817–827. https://doi.org/10.1142/S0129183191001037.

Please cite this article in press as: Kreysing et al., Passage of the HIV capsid cracks the nuclear pore, Cell (2025), https://doi.org/10.1016/j.cell.2024.12.008

CellPress
OPEN ACCESS

STAR★METHODS

KEY RESOURCES TABLE

REAGENT or RESOURCE	SOURCE	IDENTIFIER
Antibodies		
Anti-HIV-1 CA (rabbit polyclonal)	In-house; Welker et al.[51] https://doi.org/10.1128/jvi.74.3.1168-1177.2000	N/A
Anti-Lamin A/C (mouse monoclonal)	Santa Cruz Biotechnology	Cat#:sc-7292; RRID:AB_627875
Anti-FXFG-Nups (Mab414) (mouse monoclonal)	Abcam	Cat#:ab24609; RRID:AB_448181
Anti-rabbit IgG Alexa Fluor 488 (donkey polyclonal)	Thermo Fisher Scientific	Cat#:A-21206; RRID:AB_2535792
Anti-mouse IgG Alexa Fluor 647 (donkey polyclonal)	Thermo Fisher Scientific	Cat#A-31571; RRID:AB_162542
Anti-rabbit IgG Atto 594 (goat polyclonal)	Merck	Cat#:77671; RRID:AB_1137663
Anti-mouse IgG Abberior® STAR RED (goat polyclonal)	Merck	Cat#:52283; RRID:AB_3068620
Bacterial and virus strains		
HIV-1_{NL4-3} ΔEnv	Bejarano et al.[20] https://doi.org/10.7554/eLife.41800	N/A
NNHIV (HIV-1_{NL4-3} $IN_{D64N/D116N}$ $tat_{Δ33-64bp}$) ΔEnv	This paper	N/A
Biological samples		
human peripheral blood mononuclear cells (PBMC) isolated from buffy coats of healthy donors	This paper	N/A
Chemicals, peptides, and recombinant proteins		
ACCUTASE™	Stemcell Techologies	# 07920
Hoechst33258	Thermo Fisher Scientific	Cat#:H3569
Critical commercial assays		
Lowicryl® HM20 Embedding Kit	Polysciences, Inc.	Cat#:15924-1
Deposited data		
MDM-infected dataset: HIV-1 CA virion hexamer	This paper	EMDB: EMD-51531 https://www.ebi.ac.uk/emdb/EMD-51531
MDM-infected dataset: HIV-1 CA cytoplasmic hexamer	This paper	EMDB: EMD-51532 https://www.ebi.ac.uk/emdb/EMD-51532
MDM-infected dataset: HIV-1 CA inside NPC hexamer	This paper	EMDB: EMD-51533 https://www.ebi.ac.uk/emdb/EMD-51533
MDM-infected dataset: HIV-1 CA nuclear hexamer	This paper	EMDB: EMD-51534 https://www.ebi.ac.uk/emdb/EMD-51534
MDM-infected dataset: HIV-1 CA virion pentamer	This paper	EMDB: EMD-51535 https://www.ebi.ac.uk/emdb/EMD-51535
MDM-infected dataset: HIV-1 CA cytoplasmic pentamer	This paper	EMDB: EMD-51536 https://www.ebi.ac.uk/emdb/EMD-51536
MDM-infected dataset: CR subunit of NPC	This paper	EMDB: EMD-51626 https://www.ebi.ac.uk/emdb/EMD-51626
MDM-infected dataset: IR subunit of NPC	This paper	EMDB: EMD-51627 https://www.ebi.ac.uk/emdb/EMD-51627
MDM-infected dataset: NR subunit of NPC	This paper	EMDB: EMD-51628 https://www.ebi.ac.uk/emdb/EMD-51628
MDM-infected dataset: LR subunit of NPC	This paper	EMDB: EMD-51629 https://www.ebi.ac.uk/emdb/EMD-51629
MDM-infected dataset: basket attachment to NR of NPC	This paper	EMDB: EMD-51630 https://www.ebi.ac.uk/emdb/EMD-51630

(*Continued on next page*)

Continued

REAGENT or RESOURCE	SOURCE	IDENTIFIER
MDM-infected dataset: asymmetric subunit of NPC	This paper	EMDB: EMD-51631 https://www.ebi.ac.uk/emdb/EMD-51631
MDM-infected dataset: C8-symmetrized composite NPC	This paper	EMDB: EMD-51632 https://www.ebi.ac.uk/emdb/EMD-51632
MDM-mock infected dataset: CR subunit of NPC	This paper	EMDB: EMD-52138 https://www.ebi.ac.uk/emdb/EMD-52138
MDM-mock infected dataset: IR subunit of NPC	This paper	EMDB: EMD-52139 https://www.ebi.ac.uk/emdb/EMD-52139
MDM-mock infected dataset: NR subunit of NPC	This paper	EMDB: EMD-52140 https://www.ebi.ac.uk/emdb/EMD-52140
MDM-mock infected dataset: LR subunit of NPC	This paper	EMDB: EMD-52141 https://www.ebi.ac.uk/emdb/EMD-52141
MDM-mock infected dataset: basket attachment to NR of NPC	This paper	EMDB: EMD-52142 https://www.ebi.ac.uk/emdb/EMD-52142
MDM-mock infected dataset: asymmetric subunit of NPC	This paper	EMDB: EMD-52143 https://www.ebi.ac.uk/emdb/EMD-52143
MDM-mock infected dataset: C8-symmetrized composite NPC	This paper	EMDB: EMD-52144 https://www.ebi.ac.uk/emdb/EMD-52144
MDM-infected dataset: raw tilt series, inputs for tomogram reconstruction, bin4 tomograms	This paper	EMPIAR: EMPIAR-12454 https://www.ebi.ac.uk/empiar/EMPIAR-12454
MDM-mock infected (control) dataset: raw tilt series, inputs for tomogram reconstruction, bin4 tomograms	This paper	EMPIAR: EMPIAR-12457 https://www.ebi.ac.uk/empiar/EMPIAR-12457
Code for data analysis	This paper	Part of cryoCAT; Zenodo: https://doi.org/10.5281/zenodo.13916774
MD simulation files of HIV-1 capsid and NPC	This paper	Zenodo: https://doi.org/10.5281/zenodo.14179289
Experimental models: Cell lines		
Human: embryonic kidney 293T cells (HEK293T)	Pear et al.[52] https://doi.org/10.1073/pnas.90.18.8392	RRID:CVCL_0063
Oligonucleotides		
NL4-3 ΔEnv forward primer CAGACAGGCCTCG TCCAAAGGTATCCTTTGAG	This paper	N/A
NL4-3 ΔEnv reverse primer CAGACGCT AGCTATCTGTTTTAAAGTGGCATTC	This paper	N/A
Recombinant DNA		
pNNHIV	Zila et al.[24] https://doi.org/10.1016/j.cell.2021.01.025	N/A
pNNHIVΔEnv	This paper	N/A
pNL4-3ΔEnv	Bejarano et al.[20] https://doi.org/10.7554/eLife.41800	N/A
pEnv-4059	Schnell et al.[53] https://doi.org/10.1371/journal.ppat.1002286	N/A
pVpr-IN.eGFP	Albanese et al.[54] https://doi.org/10.1371/journal.pone.0002413	N/A
pVpr.IN$_{D64N/D116N}$.mScarlet	Zila et al.[24] https://doi.org/10.1016/j.cell.2021.01.025	N/A
Software and algorithms		
Volocity 6.3	Perkin Elmer	RRID:SCR_002668
Imspector 16.1.6905	Abberior Instruments	RRID:SCR_015249
Huygens	Scientific Volume Imaging	RRID:SCR_014237
Imaris	Bitplane AG	RRID:SCR_007370

(*Continued on next page*)

Continued

REAGENT or RESOURCE	SOURCE	IDENTIFIER
Fiji 2.1.0/1.53c	Schindelin et al.[55] https://doi.org/10.1038/nmeth.2019	RRID:SCR_002285
SerialEM 3.7.9 and 4.0.20	Mastronarde[56] https://doi.org/10.1016/j.jsb.2005.07.007	RRID:SCR_017293
IMOD 4.9.4 and 4.11.5	Kremer et al.[57] https://doi.org/10.1006/jsbi.1996.0013	RRID:SCR_003297
Icy 2.0.3.0	de Chaumont et al.[58] https://doi.org/10.1038/nmeth.2075	RRID:SCR_010587
ec-CLEM (Icy plugin) 1.0.1.5	Paul-Gilloteaux et al.[59] https://doi.org/10.1038/nmeth.4170	N/A
Amira 2019.3	Thermo Fisher Scientific	RRID:SCR_007353
Prism 9.5.0	GraphPad Software Inc.	RRID:SCR_002798
napari: a multi-dimensional image viewer for Python [software]	napari contributors[60] https://doi.org/10.5281/zenodo.13859720	RRID:SCR_022765
UCSF ChimeraX 1.8	Goddard et al.[61] https://doi.org/10.1002/pro.3235	RRID:SCR_015872
Artiax (ChimeraX plugin) 0.4	Ermel et al.[62] https://doi.org/10.1002/pro.4472	N/A
Relion 3.1	Zivanov et al.[63] https://doi.org/10.7554/eLife.42166	RRID:SCR_016274
novaCTF	Turoňová et al.[64] https://doi.org/10.1016/j.jsb.2017.07.007	N/A
Fourier3D	Turoňová[65] https://doi.org/10.5281/zenodo.3973621	N/A
novaSTA	Turoňová[66] https://doi.org/10.5281/zenodo.5921012.	N/A
AreTomo 1.33	Zheng et al.[67] https://doi.org/10.1016/j.yjsbx.2022.100068	N/A
GAPStop(TM)	Turoňová[68] https://doi.org/10.5281/zenodo.10822455	N/A
cryoCAT	Turoňová[50] https://doi.org/10.5281/zenodo.13916774	N/A
SWISS-MODEL	Waterhouse et al.[69] https://doi.org/10.1093/nar/gky427	RRID:SCR_018123
LAMMPS	Plimpton et al.[70] https://doi.org/10.1006/jcph.1995.1039	N/A
GROMACS	Abraham et al.[71] https://doi.org/10.1016/j.softx.2015.06.001	RRID:SCR_014565
VMD	Humphrey et al.[45] https://doi.org/10.1016/0263-7855(96)00018-5	RRID:SCR_001820
Other		
Sapphire discs, 3 × 0.05 mm	Wohlwend GmbH, Switzerland	Cat#:405
Specimen carrier, aluminum 3 × 0.5 mm, Flat / Cavity 0.3 mm	Wohlwend GmbH, Switzerland	Cat#:242
Specimen carrier, aluminum 3 × 0.5 mm, Cavity 0.1 / 0.2 mm	Wohlwend GmbH, Switzerland	Cat#:241
EM grids, copper, 2 × 1 mm slot, formvar support	Electron Microscopy Sciences	Cat#:FF2010-CU
Attofluor™ Cell Chamber	Thermo Fisher Scientific	Cat#:A7816
TetraSpeck™ Microspheres, 0.1 μm	Thermo Fisher Scientific	Cat#:T7279
Nikon Ti Perkin Elmer Ultra VIEW VoX 3D	Perkin Elmer	N/A
775 nm Expert Line STED system	Abberior Instruments GmbH	N/A
Olympus IX83 microscope	EVIDENT	N/A

(*Continued on next page*)

Continued

REAGENT or RESOURCE	SOURCE	IDENTIFIER
Olympus UPlanSApo 100× oil immersion objective (NA 1.4)	EVIDENT	N/A
EM AFS2 freeze-substitution device	Leica Microsystems	N/A
HPM010 high pressure freezer	BAL-TEC	N/A
EM UC7 ultramicrotome	Leica Microsystems	N/A
PerkinElmer UltraVIEW VoX 3D spinning-disc confocal microscope	Perkin Elmer	N/A
Tecnai TF20 electron microscope	FEI	N/A
Eagle CCD camera	FEI	N/A
Quantifoil EM gold grids, 200-mesh, R 2/2 holey carbon film	Quantifoil	N/A
EM GP2 Automatic Plunge Freezer	Leica Microsystems	N/A
Aquilos 2 cryo-FIB-SEM microscope	Thermo Fisher Scientific	N/A
Titan Krios G4 cryo electron microscope	Thermo Fisher Scientific	N/A
Falcon 4 direct electron detector	Thermo Fisher Scientific	N/A
Selectris X imaging filter	Thermo Fisher Scientific	N/A

EXPERIMENTAL MODEL AND STUDY PARTICIPANT DETAILS

Human embryonic kidney 293T cells (HEK293T)[52] were maintained in Dulbecco's modified Eagle medium (DMEM; Thermo Fisher Scientific) supplemented with 10% fetal bovine serum (FBS; Capricorn Scientific GmbH, Germany), 100 U/ml penicillin and 100 mg/ml streptomycin (Thermo Fisher Scientific). Monocyte-derived macrophages (MDMs) were obtained from human peripheral blood mononuclear cells (PBMC) isolated from buffy coats of healthy donors as described previously.[20] Buffy coats were obtained from anonymous blood donors at the Heidelberg University Hospital Blood Bank according to the regulations of the local ethics committee. MDM were cultivated in RPMI 1640 medium (Thermo Fisher Scientific) supplemented with 10% heat inactivated FBS, antibiotics (as above), and 5% human AB serum (Capricorn Scientific GmbH, Germany). Cells were cultivated at 37°C in a humidified incubator with a 5% CO_2 atmosphere. For seeding, MDM were detached by Accutase (StemCell Technologies) according to the manufacturer's instructions.

METHOD DETAILS

Plasmids

Plasmid pNNHIV for production of non-infectious, reverse transcription competent HIV-1 particles,[24] the proviral plasmids pNL4-3[72] and pNL4-3ΔEnv,[20] and the Vpr.IN$_{D64N/D116N}$.mScarlet fusion protein encoding plasmid pVpr.IN$_{D64N/D116N}$.mScarlet[24] were described previously. Plasmid pEnv-4059 encoding an R5-tropic Env from a clinical HIV-1 isolate,[53] was kindly provided by R. Swanstrom (University of North Carolina, Chapel Hill, NC, USA). Plasmid pVpr.IN.eGFP encoding a Vpr.IN.eGFP fusion protein with an HIV-1 protease recognition site between Vpr and IN,[54] was kindly provided by A. Cereseto (CIBIO, Mattareo, Italy). Plasmid pNNHIVΔEnv contains a 1 bp fill-in of an StuI site in the *env* ORF resulting in a frameshift and premature stop codon (primers used for PCR: forward, 5'-CAGAC AGGCCTCGTCCAAAGGTATCCTTTGAG-3'; reverse, 5'-CAGACGCTAGCTATCTGTTTTAAAGTGGCATTC-3').

Antibodies

For immunofluorescence staining, rabbit polyclonal antiserum against HIV-1 CA raised against purified recombinant protein (in house),[51] mouse monoclonal antibody against human lamin A/C (sc-7292; Santa Cruz), mouse monoclonal antibody against Nup153 (ab24700; Abcam) and mouse monoclonal antibody against FG-Nups (Mab414) (ab24609; Abcam) were used at a dilution of 1:1,000, 1:100 and 1:200, respectively. For spinning disc confocal microscopy, secondary antibodies donkey anti-rabbit IgG and donkey anti-mouse IgG conjugated with Alexa Fluor 488 and 647 (Thermo Fisher Scientific), respectively, were used at 1:1,000 dilution. For STED microscopy, secondary antibodies goat anti-rabbit IgG and goat anti-mouse IgG conjugated with Atto 594 (Merck; 77671) and Abberior® STAR RED (Merck; 52283), respectively, were used at 1:200 dilution.

Virus and virus-like particles

HIV-1 virions and non-infectious virus-like particles were produced in HEK293T cells grown on 175 cm^2 tissue culture flasks (side bottom) transfected with respective plasmids (total 70 μg DNA per flask) using calcium phosphate transfection. For production of infectious R5-tropic HIV-1, cells were transfected with pNL4-3ΔEnv and pEnv-4059 at a molar ratio of 4.5:1. To produce IN.eGFP labeled R5-tropic HIV-1, cells were transfected with pNL4-3ΔEnv, pVpr.IN.eGFP and pEnv-4059 at a molar ratio of 4.5:1:1. For production of

non-infectious IN.mScarlet labeled R5-tropic NNHIV, cells were transfected with pNNHIVΔEnv, pVpr.IN$_{NN}$.mScarlet and pEnv-4059 at a molar ratio of 4.5:1:1. Medium was changed 6 h after transfection and cells were further incubated at 37°C and 5% CO_2. At 44 h post-transfection, culture media from virus-producing cells were harvested and cleared by filtration through a 0.45 μm nitrocellulose filter (Carl Roth, Germany), and particles from media were concentrated by ultracentrifugation through a 20% (w/w) sucrose cushion for 90 min at 27,000 rpm (at 4°C) in a Beckman SW32 rotor (Beckman Coulter Life Sciences). Particles were resuspended either in PBS or in PBS containing 10% FBS and 10 mM HEPES (pH 7.2), then aliquoted and stored at –80°C. Particle-associated RT activity was determined by SYBR Green-based Product-Enhanced Reverse Transcription assay (SG-PERT).[73]

Sample preparation for confocal and STED microscopy

MDM seeded in 8-well μ-Slides with a glass bottom (ibidi GmbH, Germany) were infected with non-labeled or fluorescently labeled wild-type HIV-1 or NNHIV (5–15 μUnits of RT/cell) pseudotyped with R5-tropic 4059 Env and incubated at 37°C until indicated time post-infection. For both spinning disc confocal and super-resolution STED microscopy, samples were fixed with 4% FA in PBS (15 min), rinsed with PBS, permeabilized with 0.5% Triton X-100 in PBS (5–20 min) and washed three times (5–10 min) with PBS. For detection of nuclear HIV-1 CA, cells were further extracted using ice-cold methanol for 10 min (at –20°C) and subsequently washed twice with 3% bovine serum albumin (BSA) in PBS. Samples were blocked with 3% BSA in PBS for 30 min and staining with primary and secondary antibodies (both diluted in 0.5% BSA in PBS) was carried out at room temperature for 1 h each. When relevant, cell nuclei were visualized by DNA staining with 0.2 μg/ml Hoechst33258 (Thermo Fisher Scientific) in PBS for 30 min.

Spinning disc confocal microscopy

Spinning disc confocal microscopy (SDCM) was performed using a Nikon Ti Perkin Elmer Ultra VIEW VoX 3D spinning disk confocal microscope (Perkin Elmer, MA, USA) equipped with a 100× oil immersion objective (NA 1.4; Nikon) and EM-CCD ImageEM X2 camera (Hamamatsu Photonics K.K., Japan). Multichannel z series of randomly selected cells were acquired with a z-spacing of 200 nm and excitation with the 405-, 488-, 561-, and 640-nm laser lines, using the Volocity software (Perkin Elmer, MA, USA).

STED microscopy

Stimulated emission depletion (STED) imaging was performed with a 775 nm Expert Line STED system (Abberior Instruments GmbH, Germany) equipped with an SLM-based easy3D module and an Olympus IX83 microscope (EVIDENT, Tokyo, Japan) using a 100× oil immersion objective (NA 1.4; Olympus UPlanSApo, (EVIDENT, Tokyo, Japan)). Dual-color STED images were acquired line sequentially, using the 590- and 640-nm excitation laser lines and two APD spectral detectors set to collect photons with the wavelength between 590–630 nm and 650–720 nm, respectively. Acquisitions using 405- and 488-nm laser lines were in confocal mode only. Nominal STED laser power was set to 15–40% of the maximal power of 3 W with 10 μs pixel dwell time, 15 nm pixel size and 9× accumulation. Acquired STED images were deconvoluted with Huygens Deconvolution software (Scientific Volume Imaging) using Classic Maximum Likelihood Estimation (CMLE) algorithm and Deconvolution Express mode with 'Conservative' settings. For 3D STED data acquisition, 30% of the STED laser power was used for fluorescence depletion in the Z-axis and RESCue illumination scheme was used to minimize bleaching. Sampling frequency was 20 nm in xy axis and 70 nm in z. For sampling of the entire nuclear volume (~6–10 μm along the optical axis) by 3D STED, 80–150 super-resolved images were acquired. The bleaching during the acquisition was reduced by implementing a light dose management (DyMIN) that specifically activates and modulates the intensity of the STED depletion laser beam to switch off fluorophores only near the fluorescent feature to be recorded.[74]

Image analysis

Quantification of CA signals localized at the nuclear envelope or inside the nucleus of infected MDM visualized by SDCM was performed using the Icy software.[58] The volumes of individual HIV-1 CA signals in acquired z-stacks were automatically detected using the spot detector function. Objects displaying positive signal in the laminA/C or Hoechst channel were classified as nuclear envelope (NE) associated or as intranuclear, respectively. Nuclear signals were further visually examined and manually currated to ensure that objects located in nuclear regions with very low or undetectable Hoechst staining were not excluded from the analysis.

To determine percentage of CA signals colocalizing with FG-Nups at the nuclear perihery in infected MDM visualized by 3D STED, deconvoluted z-stacks were reconstructed using the Imaris software (Bitplane AG, Switzerland). Individual HIV-1 CA signals were automatically detected using the spot detector Imaris module, creating for each distinct fluorescent signal a 3D ellipsoid object with Z axis = 1.5*X,Y axis. For all objects in the proximity of NE, the median signal intensity within objects was quantified for the FG-Nups channel. All objects representing CA signals that had maximum FG-Nups signal intensity higher than 50 (a.u.) were scored as co-localizing. The same threshold was applied to all four datasets. To quantify the total amounts of nuclear pores per nucleus, individual FG-Nups signals were automatically detected by spot detector module as above and counted. To estimate the NPC density, the dimensions of nuclei mid-sections was measured using the Fiji software[55] and the surface area of each nucleus was then calculated as the surface of ellipsoid.

Sample preparation for CLEM

4 × 10^4 MDM were seeded on carbon-coated sapphire discs (Engineering Office M. Wohlwend, Switzerland) placed in a glass-bottomed 'microwell' of 35 mm MatTek dish (MatTek, Ashland, MA, USA) and cultured for 16–24 h at 37°C. Cells were infected

with IN.mScarlet labeled NNHIV particles pseudotyped with R5-tropic 4059 Env at 60 μU RT/cell. At 48 h p.i., infected cells were cryo-immobilized by high pressure freezing using a HPM010 high pressure freezer (BAL-TEC, Balzers, Liechtenstein) and discs with frozen cells were transferred to freeze-substitution medium (0.1% uranyl acetate, 2.3% methanol and 1% H_2O in Acetone) at –90°C. Subsequent freeze-substitution and embedding of samples in Lowicryl HM20 resin (Polysciences, Inc., USA) was performed in an EM AFS2 freeze-substitution device (Leica Microsystems) equipped with a EM FSP robotic solution handler (Leica Microsystems) according to Kukulski et al.,[75] modified as follows: Samples were incubated in FS medium for 5 h at –90°C and temperature was then raised to –45°C (at 7.5°C/h). Samples were washed with acetone (3 × 25 min) and infiltrated with increasing concentrations of Lowicryl HM20 in acetone (25, 50% and 75%; 3 h each), while raising temperature to –25°C (3.3°C/h). The acetone-resin mixture was replaced by pure Lowicryl HM20 for 1 h and the resin was exchanged three times (3, 5 and 12 h). Samples were polymerized under UV light for 24 h at –25°C and polymerization continued for an additional 24 h while the temperature was raised to 20°C (at 3.7°C/h).

CLEM and electron tomography

250-nm thick resin sections were obtained using an EM UC7 ultramicrotome (Leica Microsystems) and placed on slot (1 × 2 mm) EM copper grids covered with a formvar film (Electron Microscopy Sciences, FF2010-Cu). Grids were placed (section face-down) for 10 min on 20 μL drops of 1 × PHEM buffer (pH 6.9) containing 0.1 μm TetraSpeck beads (1:25) (Thermo Fisher Scientific) serving as fiducial markers and 10 μg/ml Hoechst33258 (Thermo Fisher Scientific) to stain nuclear regions in cell sections. Unbound fiducials were washed off on several drops of water and grids were transferred on 25 mm glass coverslips mounted in a water-filled ring holder for microscopy (Attofluor cell chamber, Thermo Fisher Scientific). Z stacks of sections were acquired with a PerkinElmer UltraVIEW VoX 3D spinning-disc confocal microscope (Perkin Elmer, MA, USA) and then visually examined using the Fiji software[55] to identify regions of interest (ROIs). Sections on EM grids were stained with 3% uranyl acetate (in 70% methanol) and lead citrate. Individual grids were placed in a high-tilt holder (Fischione Model 2040) and loaded to a Tecnai TF20 electron microscope (FEI) operated at 200 kV, equipped with a field emission gun and a 4K-by-4K pixel Eagle CCD camera (FEI). To map all cell sections on grid, a full grid map was acquired using the SerialEM software (version 3.7.9).[56] To identify ROIs in resin cell sections for image acquisitions, EM images and imported SDCM images were pre-correlated in SerialEM using the fiducials as landmark points[76] and single-axis tilt series were acquired in correlated positions using SerialEM with a tilt range from –60° to +60°, angular increment of 1° and a nominal pixel size of 1.13 nm. Alignments and 3D reconstructions of tomograms were done with IMOD software (version 4.9.4).[57] High precision post-correlation was performed using eC-CLEM plugin[59] in Icy software.[58]

Quantitative image analysis of capsids acquired by CLEM-ET

Segmentation, isosurface rendering and quantitative analysis of the capsid interior were done in the Amira software (Thermo Fisher Scientific) as described in Zila et al.[24] Briefly, to exclude the CA layer density from the interior of manually segmented capsid, the 'erosion' algorithm was used to shrink the volume of segmented structure. The interior voxel intensity median in shrunken volume was then determined using the 'label analysis' function and normalized to intensity median of 3–5 volumes placed in the proximity of the structure. Only structures fully covered in the EM section (not truncated at the section edge) were included in the analysis.

MDM vitrification and cryo-FIB milling

MDM were detached by accutase (StemCell Technologies) according to the manufacturer's instructions. 4×10^4 MDM were seeded on glow discharged and UV-light sterilized 200-mesh EM gold grids coated with R 2/2 holey carbon films (Quantifoil Micro Tool GmbH), which were placed in a glass-bottomed 'microwell' of 35-mm MatTek dish (MatTek, Ashland, MA, USA). After seeding, cells were cultured for an additional 24 h at 37 °C. For infection, cells were incubated with IN.mScarlet labeled NNHIV particles pseudotyped with R5-tropic 4059 Env at 60 μU RT/cell for 48 hours. Mock-infected and infected MDM were vitrified by plunge freezing into liquid ethane at –183°C using an EM GP2 plunger (Leica Microsystems). The blotting chamber was maintained at 37°C temperature and 90% humidity. Before plunge freezing, 3 μl of culture medium were applied onto grids. Subsequently, the grids were blotted from the back side for 3 s with a Whatman filter paper, Grade 1, and plunge frozen. The samples were then cryo-FIB milled using an Aquilos 2 microscope (Thermo Fisher Scientific) similar to a previously described workflow.[77] In brief, samples were coated with an organometallic platinum layer using a gas injection system for 10 sec and additionally sputter coated with platinum at 1 kV and 10 mA current for 10 sec. Milling was performed with AutoTEM (version 2.4.2) (Thermo Fisher Scientific) in a stepwise manner with an ion beam of 30 kV while reducing the current from 1000 pA to 50 pA. Final polishing was performed with 30 pA current with a lamellae target thickness of 200 nm.

MDM cryo-ET data acquisition

Cryo-ET data for infected and control macrophages were collected at 300 kV on a Titan Krios G4 microscope (Thermo Fisher Scientific) equipped with a E-CFEG, Falcon 4 direct electron detector (Thermo Fisher Scientific) operated in counting mode and Selectris X imaging filter (Thermo Fisher Scientific). For each grid, montaged grid overviews were acquired with 205 nm pixel size. Montages of individual lamellae were taken with a 3 nm pixel size. Tilt series were acquired using SerialEM (version 4.0.20)[56] in low dose mode as 4K x 4K movies of 10 frames each and on-the-fly motion-corrected in SerialEM. The magnification for projection images of 53000x corresponded to a nominal pixel size of 2.414 Å. Tilt series acquisition started from the lamella pretilt of ± 8° and a dose-symmetric

acquisition scheme[78] with 2° increments grouped by 2 was applied, resulting in 61 projections per tilt series with a constant exposure time and targeted total dose of ~135 e^- per $Å^2$. The energy slit width was set to 10 eV and the nominal defocus was varied between -2.0 to -4.0 μm. Dose rate on the detector was targeted to be ~4-6 e^- /px/sec.

Tomogram reconstruction

The motion corrected tilt series were corrected for dose exposure as previously described [79] using a Matlab implementation that was adapted for tomographic tilt series.[80] Projection images with poor quality were removed after visual inspection. The dose-filtered tilt series were then aligned with patch-tracking in AreTomo (version 1.33)[67] and reconstructed as back-projected tomograms with SIRT-like filtering of 15 iterations at a binned pixel size of 9.656 Å (bin4) in IMOD (version 4.11.5)[57] From the reconstructed tomograms, those containing nuclear pore complexes and/or HIV capsids were selected by visual inspection.

The same tomograms were also reconstructed with 3D-CTF correction using novaCTF[64] with phase-flip correction, astigmatism correction and 30 nm slab. Tomograms were binned 2x, 4x and 8x using Fourier3D.[65]

HIV CA hexamer subtomogram averaging

Capsid-like structures were identified in the infected macrophage SIRT-like filtered bin4 tomograms and then manually segmented in napari.[60] The segmentation was used to create a convex hull with the cryoCAT package.[50] Subtomogram averaging of the capsid hexamer was performed similarly to a previously described protocol.[15] In detail, first the segmented capsid surfaces (at 4x binning) were oversampled with a sampling distance of 2 voxels and each position was assigned an initial orientation that was determined based on the normal vector of the segmented cone surface at given position (the in-plane angle was assigned randomly). Then the coordinates were multiplied by factor of 2 to obtain positions for bin2 tomograms. All subsequent subtomogram alignment and averaging was performed with imposed C6 symmetry in novaSTA.[66] For virion capsids, the oversampled positions of four capsids were used to extract bin2 subtomograms from 3D-CTF corrected tomograms. These subtomograms were used to generate an initial featureless average and then aligned for six iterations. A distance threshold of 16 voxels was used to remove overlapping subtomograms (i.e. particle duplicates). Low CCC threshold and/or incorrect orientation (both assessed visually using ArtiaX[62]) lead to additional removal of subtomograms. The resulting subtomograms, now split into halfsets, were then aligned for six iterations to obtain a better average and lattice arrangement. After further removal of suboptimal positions, the final subtomograms were again aligned for six iterations.

This STA map of the virion hexamer was then used as an existing reference (lowpass filtered to 40 Å) to align all oversampled virion capsid positions and obtain more complete lattices. The resulting positions were used to remove duplicates and suboptimal positions as described above. As before, the dataset was split into halves at this point. After multiple iterations of subtomogram alignment, removal of incorrectly oriented positions and then manual addition of potential positions to complete the lattice again in ArtiaX,[62] a final removal of incorrectly oriented positions was performed. The final subtomograms were again aligned for nine iterations (for final particle numbers see Table S1).

For capsids in the cytoplasm, inside NPCs or in the nucleus, the same procedure was applied.

The FSC calculations for each dataset were performed in Relion (v3.1)[63] and plotted using Python. The resolution was evaluated at FSC=0.5 and not FSC=0.143 due to manual addition of particles, as described above, after initial splitting into halfsets.

HIV CA pentamer subtomogram averaging

All subsequent subtomogram alignment and averaging was performed with imposed C5 symmetry in novaSTA.[66] Positions and orientations for subtomogram averaging of the CA pentamer were obtained by placing particles into the areas of the capsid lattice where hexamers were arranged around a pentamer hole as visualized in ArtiaX.[62] Virion candidate positions were processed separately from cytoplasmic and inside NPC candidate positions. In each case, the candidate positions were used to extract bin2 subtomograms from 3D-CTF corrected tomograms. These subtomograms were used to generate an initial featureless average and then aligned for nine iterations. Low CCC threshold and/or incorrect orientation (both assessed visually using ArtiaX[62]) led to additional removal of subtomograms. The final subtomograms were aligned for nine iterations (for final particle numbers see Table S1). Due to the low particle numbers for pentamers which prevented obtaining reasonable halfmaps, the FSC calculations were done in a different manor. Here, the virion pentamer was treated as halfmap1 and EMD-3466[15] as halfmap2 and the resolution evaluated at FSC=0.5. The cytoplasmic pentamer map was treated as halfmap1 and EMD-12457[39] as halfmap2 and the resolution evaluated at FSC=0.5. The FSC calculations for each dataset were performed in Relion (v3.1)[63] and plotted using Python.

HIV CA pentamer template matching

A published CA pentamer STA map (EMD-3466[15]) was downsampled to a pixel size of 4.828 Å (bin2 for this dataset) and then used as a search template to perform template matching in parts of a bin2 tomogram with capsid-like structures using GAPSTOP™.[42,68] The angular search range was set to 5-degree angular sampling. The highest CCC peaks from template matching were extracted with their corresponding orientations and then visually inspected in ArtiaX[62] to obtain only the plausible candidates that are oriented correctly to the capsid surface as visible in the tomogram. These positions were then used for modeling of the capsid for MD simulations as described in *In-situ capsid modeling*.

Please cite this article in press as: Kreysing et al., Passage of the HIV capsid cracks the nuclear pore, Cell (2025), https://doi.org/10.1016/j.cell.2024.12.008

NPC particle selection and subtomogram averaging

Positions of NPCs were manually selected in the bin4 SIRT-like filtered tomograms as described previously.[81] Extraction of particles from the novaCTF-corrected tomograms, subtomogram alignment and averaging was performed using novaSTA.[66] NPC averaging was performed as described previously.[26] First, an average of the whole NPC was obtained while utilizing C8 symmetry and a cylindrical mask. Next, coordinates of the subunits were extracted based on the aligned positions using C8 symmetry while also splitting the dataset into halves. With these subunit positions an average structure of the asymmetric unit of the NPC was obtained using an elliptical mask. To obtain averages of individual NPC rings, first particle positions were re-centered to the respective area (CR, IR, NR, LR, nuclear basket) based on their position in the subunit average. Then the newly extracted bin4 subtomograms for the individual rings were aligned and averaged with elliptical masks. To generate C8 symmetric composite NPC maps, first the final averages of individual ring maps were fitted into the asymmetric subunit average. Then the composite map was created by applying symmetry based on the coordinates used for splitting the initial whole NPC average into asymmetric units. The entire NPC STA procedure was first performed for control and infected macrophage NPCs separately and then redone for the combined set of NPCs after determining no discernible difference between the two macrophage NPC structures (control and infected). The FSC calculations for each dataset were performed in Relion (v3.1)[63] and plotted using Python.

NPC diameter measurements

The NPC diameters at different points were measured based on the coordinates obtained from STA maps of individual rings (CR, IR, NR) using previously published MATLAB scripts.[26] Using ChimeraX,[61] the measurement point of interest coordinates in the individual ring average were determined with the marker tool and the particle list coordinates were offset by the shift between the center of the average and the measurement point of interest. Only NPCs with five or more subunits were considered for diameter measurement of NPCs. As previously described,[26] line segments were determined that connected opposing subunits for each individual NPC. The NPC center was defined as the point to which the distance of all line segments was minimal. The NPC radius was calculated as the distance from the center to each subunit. Data was plotted using Prism9 software (Figures S3C and S3D). Statistical significance was tested using unpaired two-tailed t test in Prism9.

NPC ring subunit template matching

The obtained bin4 STA averages for CR, IR and NR were masked to only include a single subunit and then used as search templates (lowpass filtered to 30 Å) to perform template matching in full 3D-CTF-corrected bin4 tomograms with visible NPCs using GAPSTOP™[42,68] based on the STOPGAP software package.[82] The angular search range was set to a 6-degree sampling which has been shown to increase TM performance.[42] The constrained cross-correlation (CCC) peaks which had values 7x above the mean of the CCC-volume were extracted with their corresponding orientations and then manually cleaned in the ArtiaX plugin[62] for ChimeraX[61] to obtain only plausible candidates that are oriented correctly in the nuclear envelope. This resulted in three different particle sets for CR, IR, NR with all template matched subunit coordinates and orientations for each tomogram. The association of each ring subunit to individual NPCs was determined using the cryoCAT package.[50]

NPC ring subunit interior angle of polygon (IAOP) measurements

To obtain the interior angle of the polygon (IAOP) (see Figure 5C cartoon), i.e. the rotation around the symmetry axis from a given to the neighboring subunit, in each NPC ring (CR, IR, NR) an in-house python script was used. First, the circle center for each NPC ring was determined using the cryoCAT package.[50] Here a threshold of at least four subunits per NPC ring was used to ensure accurate circle fitting. Then the angle between neighboring vectors connecting the circle center to the center of each subunit as determined by template matching was calculated. To ensure that only the direct neighbor angles were measured a threshold of 55° was applied and then only NPC rings with three or more angle measurements were included in the final analysis. To determine statistical significance of the measured angles in NPC rings between infected and control macrophages a threshold of 42.5° (the halfway point between the angle of a regular C8-symmetric NPC with 45° and the angle of a C9-symmetric NPC with 40°) was chosen. Then the number of NPCs that had a median subunit angle of less than 42.5° and those above or equal to the threshold were extracted from the data and subjected to a Fisher's exact test (Prism 9 software). Data was plotted using Python (Figures 5C and S4).

In-situ capsid modeling

A multi-step approach was employed to construct an atomic model of a complete *in situ* HIV capsid. STA for hexamers and TM for pentamers applied to a single and relatively well-resolved cone-shaped capsid yielded the centers of 141 hexamers and 8 pentamers (Figures S5A1 and S5A2). From these, the capsid surface was estimated as a convex hull (Figure S5A3) using the ArtiaX boundary method[62] in ChimeraX.[61] The position of missing points in the cone lattice were then determined by oversampling random points on the surface of the convex hull and keeping points closest to the expected positions based on the translation vectors of the existing neighbors. Those with the most neighbors were iteratively selected, adding them one-by-one to the list. Once complete, the positions of the 46 added lattice points (~24% of the total) were visually inspected and manually adjusted in ChimeraX[61] (Figure S5A4).

In the next step, the lattice was globally relaxed by annealing a coarse-grained particle model (Figure S5A5). Hexamers and pentamers were represented as beads. The six neighboring beads of hexamers, and the five of pentamers were connected by harmonic springs $\kappa(r - r_0)^2/2$ with r the pair distance, $r_0 = 9.3$ nm the distance between hexamers obtained by placing atomic models[83,84] in

the experimental STA of the hexamer which included the first neighbor, and $\kappa = 3\ \mathrm{kJ \cdot mol^{-1} \cdot nm^{-2}}$ the spring constant. In addition, the beads were softly tethered to their initial position by a potential $kd^2/2$ with d the distance and $k = 1.0\ \mathrm{kJ \cdot mol^{-1} \cdot nm^{-2}}$ the spring constant. The total energy was annealed using Gromacs 2022[71] by reducing the temperature linearly from 300 K to 10 K in 10000 steps of molecular dynamics.

Finally, the complete capsid was built by replacing each bead with atomic models of hexamers (PDB: 8CKV[83]) and pentamers (PDB: 8G6L[84]) rotated and translated according to the lattice (Figure S5A6). Missing loop residues were modeled using Swiss model.[69]

We refined the atomistic model of the in situ HIV capsid with all-atom molecular dynamics (MD) simulations of the capsid solvated in explicit water and ions at 310 K using Gromacs version 2023.4.[71] To minimize initial steric clashes at the hexamer and pentamer interfaces, we repeated the lattice annealing procedure described above with a pair distance of r_0=10.5 nm. The resulting atomic capsid model was placed in a hexagonal-prism simulation box. After performing an in-vacuum minimization using a soft-core potential, the system was solvated with TIP3P water[85] and 150 mM KCl, with ions replacing randomly selected water molecules. We further removed solvent within 4 Å of the proteins leading to a total number of 59954356 atoms. For protein and ions, we used the amber99sb*-ildn[86] and Matmakulov-Schwierz force fields,[87] respectively. The solvated system was then equilibrated in several steps. After 50,000 steps of energy minimization using the steepest descent algorithm, we performed a 0.5 ns simulation in the NVT ensemble (with fixed number of particles, volume and temperature), followed by 0.5 ns in the NPT ensemble (with fixed pressure and fluctuating volume) with position restraints on all heavy protein atoms (1000 $\mathrm{kJ \cdot mol^{-1} \cdot nm^{-2}}$) to equilibrate the solvent. Next, four consecutive 1-ns runs in the NPT ensemble were performed with decreasing position restraints (500, 200, 50, and 10 $\mathrm{kJ \cdot mol^{-1} \cdot nm^{-2}}$) to gradually remove restraints on the protein. Finally, we performed a 250 ns unrestrained MD simulation. We used a time step of 2 fs and calculated electrostatic interactions using the particle-mesh Ewald (PME) algorithm.[88] Pressure was maintained at 1 atm using the Parrinello-Rahman algorithm,[89] and temperature control was managed by the velocity-rescale algorithm.[90] Despite a slight compaction of the capsid, expected from the larger pair distance, the overall structure of the initial in situ model obtained above was maintained. Relaxations in the hexamer and pentamer interfaces resulted in an overall stable capsid.

Coarse-grained model of NPC and HIV capsid

We built coarse-grained models of the NPC and the HIV capsid in which each amino acid of the proteins is mapped into a single particle.[44] The beads are categorized as protein residues (p), membrane particles (m) and HIV capsid particles (c). The protein group has further sub-categories: scaffold residues (sc) and FG residues (FG) of NPC proteins; outer (CA) and inner (CA^i) residues of CA hexamers and CA pentamers building the HIV capsid; and the particles containing inside the HIV capsid (HIV_{in}). The potential energy of the system was given by

$$U = U_{\mathrm{LJ}} + U_{\mathrm{FENE}} = 4k_BT \sum_{i<j, r_{ij}<r_c^{\alpha}, i,j \in \{p,m\}} \left\{ \tilde{\epsilon}_{ij} \left[\left(\frac{\sigma_{ij}}{r_{ij}}\right)^{12} - \left(\frac{\sigma_{ij}}{r_{ij}}\right)^{6} \right] - U_{LJ}\left(r_c^{\alpha}\right) \right\} + 4k_BT \sum_{\langle i,j=i+1\rangle, i,j \in p, r_{ij} < 2^{\frac{1}{6}}\sigma} \left[\left(\frac{\sigma}{r_{ij}}\right)^{12} - \left(\frac{\sigma}{r_{ij}}\right)^{6} + \frac{1}{4} \right] - \sum_{\langle i,j=i+1\rangle, i,j \in p} 0.5 k_{\mathrm{FE}} R_{\mathrm{FE}}^2 \ln\left[1 - \left(\frac{r_{ij}}{R_{FE}}\right)^2\right] \quad \text{(Equation 1)}$$

The non-bonded interactions between particles i and j in all categories are modelled by Lennard-Jones (LJ) potentials, whose strength $\tilde{\epsilon}_{ij}$, length σ_{ij}, and cut-off values r_c^{α} are listed in Table S2A. The bond potential between neighboring beads along the FG-proteins is expressed by the FENE potential[91] with $k_{\mathrm{FE}} = 30k_BT$ and $R_{\mathrm{FE}} = 1.5\sigma$. All simulations were performed in LAMMPS (Release date: Sept. 2021).[70] Times are reported in units of $\tau = \sqrt{m\sigma^2/k_BT}$, with m the bead mass. Box sizes are listed in Table S2B, and MD run lengths in Table S2C.

A coarse-grained representation of the nuclear envelope separating the cytoplasm and nucleoplasm was built as described.[44] We first built a tightly packed 100x100 $\mathrm{nm^2}$ coarse-grained POPC lipid bilayer patch (command: *insane.py -l POPC -x 100 -y 100 -z 100 -a 0.3 -o bilayer.gro*). With this patch, we created a half-toroidal membrane pore using the BUMPy software[92] (command: *bumpy.py -s double_bilayer_cylinder -f bilayer.gro -z 10 -g l_cylinder:10 r_cylinder:550 r_junction:120 l_flat:2560*). We then placed particle beads at the phosphate groups of the bilayer.

For the NPC, we used the dilated NPC based on PDB: 7R5J [27] with the following FG-Nups anchored as in model II of [44]: NUP54, NUP58, NUP62, NUP98, POM121, NUP214, NUP153 and NUP358. Both NPC scaffold and membrane particles were fixed during the simulations. A LJ potential with large repulsive range prevented the escape of FG-Nups into the lumen of the nuclear envelope (Table S2A). To match experiments,[44] we set the FG-FG interaction strength to $\tilde{\epsilon}_{\mathrm{FG-FG}} = 0.42$ for all simulations unless otherwise stated. For $\tilde{\epsilon}_{\mathrm{FG-FG}} = 0.42$, FG-Nup98 (aa1-499) was found to be close to the critical point of protein condensate formation.[44] We confirmed that for $\tilde{\epsilon}_{\mathrm{FG-FG}} = 0.42$ the FG-Nup98 root mean squared extension in the dilated NPC structure used here agrees with the experimental FLIM-FRET measurements (Figure S5C).

Labelling the outer surface particles of HIV capsid

In our model, FG-Nups bind only to the outer surface of the HIV capsid. To identify the outer surface, we placed the coarse-grained HIV capsid inside a cubic box of size 441σ with 500 FG-Nup98 chains (aa1-499) and ran MD simulations using a Langevin

thermostat[93] with damping coefficient 10τ. We treated the HIV capsid as a rigid body using a rigid body integrator with a Langevin thermostat and a damping coefficient 3000τ (LAMMPS command: *fix rigid langevin molecule*). With weak interaction strengths between FG-Nup and HIV capsid particles, $\tilde{\epsilon}_{FG-FG} = \tilde{\epsilon}_{FG-CA} = 0.2$, the chains formed coil configurations and explored the outer surface of HIV capsid. We did not observe the penetration of chains into the HIV capsid. Particles within 1.5σ of the capsid were stored every 1000τ for $4.5\times10^5\tau$. We labelled an HIV capsid particle as an outer particle if it contacted at least one FG-Nup particle during the simulation. We then labelled all equivalent particles across the 182 CA hexamers and 12 CA pentamers as outer particles, and all others as inner particles. We then filled the interior of the capsid with "cargo," primarily RNA, modeled as particles on a cubic lattice (400807 particles with lattice constant $\sigma_{lattice-lattice} = 2^{-\frac{1}{6}}\sigma$). Figure S5B shows the cut view of the HIV capsid with inner lattice particles. We do not show the inner lattice particles in other figures.

Binding affinity of a strand of FG-Nup153 to CA hexamers

We estimated the effective FG-CA hexamer interaction strength by matching the calculated binding affinity of a single CA hexamer and a fragment of FG-Nup153 to the experimentally measured value.[17] A single CA hexamer and a 17-mer fragment of FG-Nup153 (aa1407-aa1423) were simulated inside a cubic box of size $60\sigma = 36$ nm. We sampled the cross interaction potential between CA hexamer and oligomer $U_{FG-CA}(t)$ every 10τ for $10^7\tau$, with pair interactions truncated and shifted at 2σ. We defined CA hexamer and oligomer as bound if the interacting energy was lower than the threshold energy: $U_{FG-CA} < U_{th}$. The probability of the bound state was calculated as $P_b = \sum_{i=1}^{N} \frac{H(U_{th} - U_{FG-CA}(t_i))}{N}$, where $N = 10^6$ is the number of sampled energies, and $H(x) = 1$ for $x > 0$ and $H(x) = 0$ otherwise is the Heaviside function. The dissociation constant as a measure of the binding affinity is calculated as $K_d = \frac{(1-P_b)^2}{N_A V P_b}$, where N_A is the Avogadro number and $V = (36\text{nm})^3$ the box volume. As shown in Figures S5D and S5E, we found that for interaction strengths close to $\tilde{\epsilon}_{FG-CA} = 0.5$ the calculated binding affinity matches the experimental value $K_d^{exp} = 49\mu M$[17] independent of threshold energy and damping coefficient of the Langevin thermostat.

Modelling cracks in NPC scaffold

We modelled a crack in the NPC scaffold by cutting its rings and pulling them apart at the seam to resemble a nine-fold symmetric scaffold. For this, the coordinates of scaffold beads *i* in the cylindrical coordinate system $\{r, \theta, z\}$ were mapped into new coordinates $\{r_n, \theta_n, z_n\}$ according to

$$r_{i,n} = \mathcal{R}\, r_i \qquad \text{(Equation 2)}$$

$$\theta_{i,n} = \begin{cases} \frac{8}{9}(\theta_i - \theta_0) + \frac{\pi}{9}, \text{for } \theta_i > \theta_0 \\ \frac{8}{9}(\theta_i - \theta_0) - \frac{\pi}{9}, \text{for } \theta_i < \theta_0 \end{cases}$$

$$z_{i,n} = z_i$$

$\mathcal{R}$ is the radial scaling factor, θ_0 is the reference angle at which the NPC scaffold is cracked and the z coordinates of the beads are kept identical as in the intact NPC. This map retains the local interactions of the structure except at the crack. For scaling factors of $\mathcal{R} = 1.2$ and $\mathcal{R} = 1.45$, the inner-ring diameters D_{in} widens from 58 nm to 69.6 nm and 84.1 nm, respectively. With $\theta_0 = 0.1031$ rad, we set the crack interface between two spokes of the NPC scaffold in our model. To fit the nuclear envelope around the new cracked NPC, we rescaled the radial coordinates of the membrane particles by factors 1.14 and 1.38 for $\mathcal{R} = 1.2$ and $\mathcal{R} = 1.45$, respectively. The resulting structures of the NPC scaffold are shown in Figures S6A–S6F.

To model the dispersion in NPC diameters seen in the experiments (Figure S3D), we built intact NPC models with different scaffold pore dimensions. For this, we radially scaled the scaffold bead positions of the intact in-cell NPC without opening a lateral void by using the mapping.

$$r_{i,n} = \mathcal{R}\, r_i \qquad \text{(Equation 3)}$$

$$\theta_{i,n} = \theta_i$$

$$z_{i,n} = z_i$$

To equilibrate the cracked and intact expanded NPCs, the FENE bond potential was initially replaced by a harmonic bond potential with $U_{har} = 0.5k_{\mathrm{harm}}\sum_{\langle i,j=i+1\rangle, i,j\in p} 0.5k_{har}(r_{ij}-\sigma)^2$, where $k_{\mathrm{harm}} = 10^4 k_B T\sigma^{-2}$ and the sum runs over all bonded neighboring beads, i.e. $\langle i, j = i+1\rangle$. The systems were equilibrated for $131\times10^3\tau$. Then the harmonic bonds were replaced with the FENE bond and the systems were equilibrated for at least $18\times10^3\tau$.

Force-driven passage of HIV capsid through NPC

We probed the passage of HIV capsids through NPCs in MD simulations with a force acting on the capsid pointing in a direction normal to the nuclear envelope. We aligned the long axis of the HIV capsid with the NPC symmetry axis. We placed the HIV capsid in the cytosol at a height of $z_i - z_C = -144$ nm of its center, where z_i is the NPC's inner-ring position. Then we applied a force $-\frac{10^{-4}k_BT}{\sigma} \approx -6.85\times10^{-4}$pN directed along the z direction toward the nucleus onto each HIV capsid particle, amounting to a total force of 0.4488 nN. The total simulation time of runs with applied force were $10^4\ \tau$. For reference, we also simulated NPCs without FG-Nups. The position of the HIV capsid center as a function of the simulation time is shown in Figures S6G–S6L for three replicas. For the intact in-cell NPC ($D_{\mathrm{in}} = 58$ nm), the HIV capsid remained stuck inside the NPC, with steric collisions blocking the translocation through the NPC scaffold even without FG-Nups. By contrast, the HIV capsid can translocate through the intact expanded NPC ($D_{\mathrm{in}} = 69.9$ nm, $\mathcal{R} = 1.2$) and cracked NPCs ($D_{\mathrm{in}} = 69.9$ nm, $\mathcal{R} = 1.2$ and $D_{\mathrm{in}} = 84.1$ nm, $\mathcal{R} = 1.45$).

Free energy profile for HIV capsid passage through NPC

We used MD simulations to determine the free energy profile for HIV capsid passage through NPCs. We extracted a set of initial configurations at different capsid positions from the MD simulations of force-driven NPC passage described above. We then fixed the HIV capsid in space and ran simulations for $188\times10^3\tau$. After $90\times10^3\tau$ of equilibration, we averaged the total force on the HIV capsid directed along the z-axis every 10τ. Figures S7A–S7C show the final configurations for different HIV capsid positions along the translocation path. Figure S7D shows the total force on the HIV capsid per CA monomer (with a total of 1152 monomers in the HIV capsid). As described in the analysis of force-driven passage, steric clashes prevent the HIV capsid from translocating beyond $z_i - z_C > -10$ nm in the intact in-cell NPC. We obtained the potential of mean force by integrating the mean force F_z along the translocation path, $\Delta F(z) = \int_{z_1}^{z} F_z(z)dz$, where z_1 is the initial position on the cytoplasmic side. For the intact in-cell NPC, numerical integration gave a free energy minimum at $z_i - z_C = -30.5$ nm. For the cracked NPCs with $D_{\mathrm{in}} = 69.9$ nm and $D_{\mathrm{in}} = 84.1$ nm, we fitted two Gaussian functions $F_z(z) = a_1 e^{-\left(\frac{z-b_1}{\sqrt{2}c_1}\right)^2} + a_2 e^{-\left(\frac{z-b_2}{\sqrt{2}c_2}\right)^2}$ to the force data with the symmetry constraint $\int_{-\infty}^{+\infty} F_z(z)dz = 0$. The fitting parameters are listed in Table S2D. For the cracked NPCs, the minima of the free energy are at $z_i - z_C = -1$ nm and 7 nm, respectively (Figure 6D).

Release and tilt of HIV capsid inside NPC

The HIV capsid was released inside intact and cracked NPCs with $\tilde{\epsilon}_{\mathrm{FG-CA}} = 0.5$. In MD simulations of at least $2\times10^5\tau$ (Table S2C), the capsid position and orientation was relaxed. The final orientations of the released HIV capsids are shown in Figure 6E.

QUANTIFICATION AND STATISTICAL ANALYSIS

The details of quantification and all statistical analyses have been described in the relevant sections of the method details.

CellPress
OPEN ACCESS

Supplemental figures

A

#	Location at NPC	Shape	Length [nm]	Width [nm]	Comment	Slicer view	Segmentation xy	Segmentation yz
1	Cy, Docking	Cone	106	61				
2	Cy, Docking	Cone	109	52				
3	Cy, Docking	Cone	135	61				
4	Cy, Docking	Cone	105	49	Figure 3B" i			
5	Cy, Docking	Cone	98	55				
6	Cy, Docking	Cone	113	50				
7	Cy, Docking	Cone	106	54				
8	Cy, Docking	Cone	108	65				
9	Cy, Docking	Cone	107	62				
10	Cy, Docking	Cone	127	53				
11	Cy, Docking	Tube	97	36				
12	Cy, Docking	Cone	116	48				
13	Cy, Docking	Cone	97	58				
14	Cy, Docking	Cone	100	66				
15	Cy, Docking	Cone	127	62				
16	Cy, Docking	Cone	102	48				
17	Cy, Docking	Cone	107	53				
18	Cy, Docking	Cone	94	46				
19	Cy, Docking	Cone	89	55				
20	Inside NPC	Cone	105	55				
21	Inside NPC	Cone	120	58				
22	Inside NPC	Cone	92	44	Figure 3A"iii			
23	Inside NPC	Cone	106	49	Figure 3A" ii			
24	Inside NPC	Cone	110	41	Figure 3A" i			
25	Inside NPC	Cone	117	49				
26	Inside NPC	Cone	119	51				
27	Inside NPC	Cone	119	57				
28	Inside NPC	Cone	104	51				
29	Inside NPC	Cone	128	57				
30	Inside NPC	Cone	108	47				
31	Inside NPC	Cone	132	59				
32	Inside NPC	Cone	106	43				
33	Nu, basket	Cone	103	51	Figure 3C i			
34	Nu, basket	Cone	115	54				
35	Nu, basket	Cone	124	57	Figure 3B" ii			
37	Nu, basket	Cone	115	58				
38	Nu, basket	Cone	114	61				
39	Nu, basket	Cone	129	52				
40	Nu, basket	Cone	110	46				
41	Nu, basket	Cone	104	50				
42	Nu, basket	Tube	93	49				
43	Nu, basket	Cone	106	44				

B

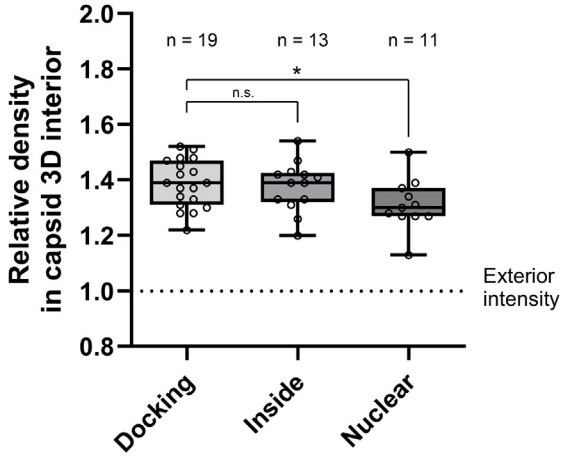

(legend on next page)

Figure S1. Overview of viral structures captured by CLEM-ET, related to Figure 3

(A) Capsids are shown as tomographic slices or manually segmented views (yellow). Indicated are capsids at cytoplasmic side of the NPC (Cy, docking), capsids penetrating the NPC (inside NPC), and capsids located at basket region of the NPC (nuclear, basket). Cy, cytoplasm; Nu, nucleus.

(B) Quantification of densities observed inside of capsids captured at NPCs of infected MDMs by CLEM-ET. For each of (*n*) segmented capsid structures the voxel intensity median within its interior was quantified and normalized to the average voxel intensity measured in the respective surrounding (dashed line) as described in STAR Methods. Whiskers represent minimum and maximum. Statistical significance was calculated using an unpaired two-tailed t test. n.s., not significant; $^{*}p = 0.0346$.

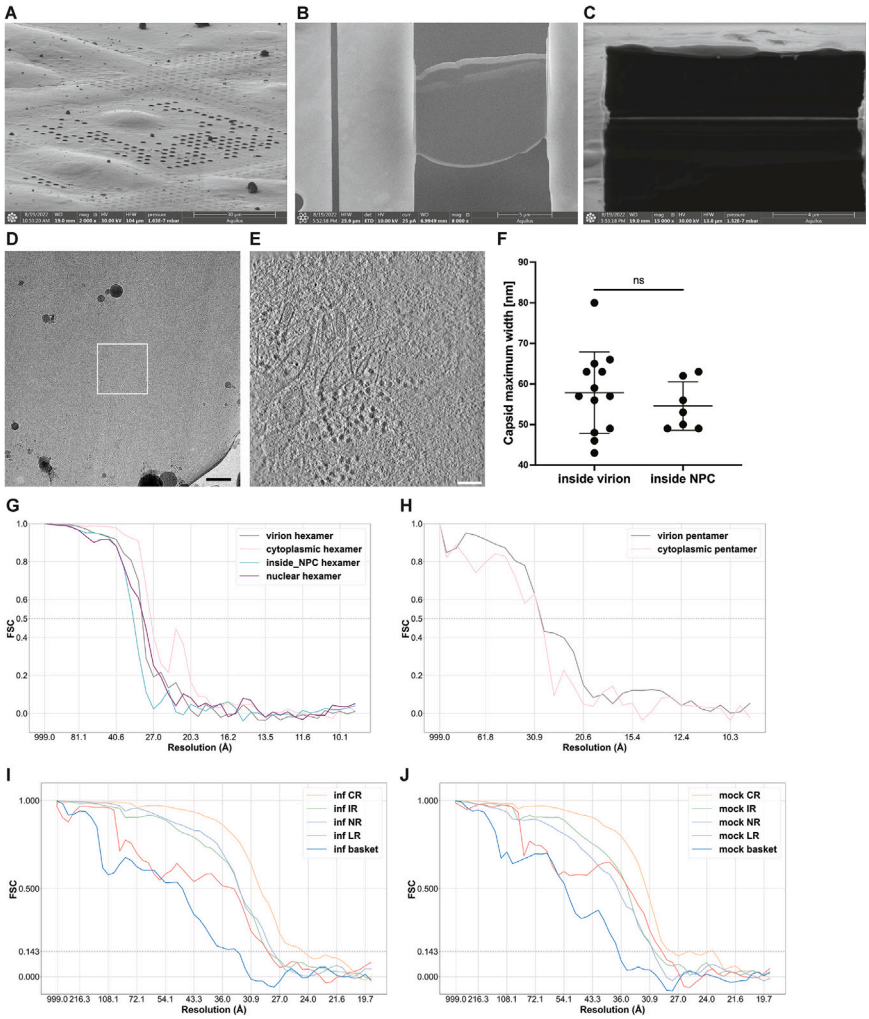

Figure S2. Cryo-ET workflow of human primary macrophages, capsid widths, and FSC curves, related to Figure 4

(A) FIB view of macrophages seeded on the EM grid.

(B) Scanning electron microscopy (SEM) view of thinned macrophage lamella.

(C) FIB view of thinned macrophage lamella.

(D) Transmission electron microscopy (TEM) medium magnification view of macrophage cell with white box highlighting acquisition area.

(E) Virtual slice through exemplary cryo-tomogram.

(F) Maximum capsid widths of HIV capsids inside virions and inside NPCs measured in IMOD slicer.[57] The mean width for capsids inside virions (57.9 nm, standard deviation = 10.0 nm) and the mean width for capsids inside NPCs (54.6 nm, standard deviation = 6.0 nm) are not statistically significantly different (unpaired two-tailed t test, ns = not significant).

(G) Fourier shell correlation (FSC) curves for HIV capsid hexamer STA maps.

(H) FSC curves for HIV capsid pentamer STA maps. Due to low particle numbers for pentamers, these FSC curves were determined by comparing the maps to published structures (see STAR Methods for details).

(I) FSC curves for NPC subunits from HIV-infected macrophages.

(J) FSC curves for NPC subunits from mock-infected macrophages. For final particle numbers and resolutions of all maps, see Table S1. Scale bar in (D) 500 nm and (E) 100 nm.

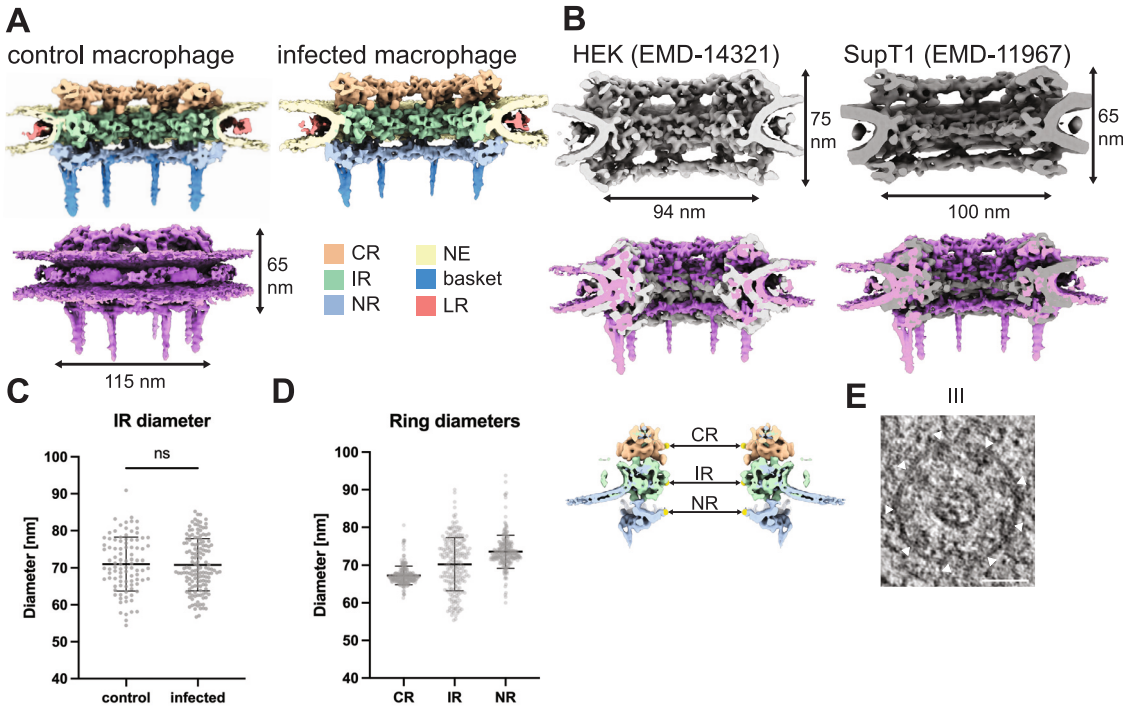

Figure S3. Comparison of NPC structure of human primary macrophages to published human NPC structures, related to Figure 5

(A) The macrophage NPC scaffold architecture is not altered in HIV-1-infected cells as compared with control cells. A side view cross section of the 8-fold symmetrized NPC STA composite map shows the individual rings/filaments color-coded. The control macrophage NPC is also shown as a full side view in pink. The reported dimensions are from the top of the CR scaffold to bottom of the NR scaffold, as the height of NPC and inner-outer membrane fusion point to opposing fusion point as width.

(B) The published NPC structure from HEK cells in light gray[27] and from SupT1 cells in dark gray[24] are shown as side view cross sections. An overlay with the control macrophage NPC structure is shown underneath each published structure. The HEK cell NPC structure is taller and less wide than either the SupT1 (intermediate width) or macrophage NPC structure (widest).

(C) The inner-ring diameters of control macrophages and infected macrophages are not significantly different. The graph below depicts the mean value and the standard deviation of the measured NPC diameters for control macrophages (mean = 71.0 nm, standard deviation = 7.2 nm, *n* = 95) and HIV-infected macrophages (mean = 70.8 nm, standard deviation = 7.0 nm, *n* = 145) as black bars with each data point shown as a gray dot. Unpaired two-tailed t test, ns = not significant.

(D) The macrophage NPC has a wider diameter across all three rings (CR, IR, NR) as compared with SupT1 cells.[24] The schematic on top shows where the diameter was measured between opposing CR, IR, NR subunits, respectively. The graphs below depict the mean value and the standard deviation of the measured NPC diameters for combined macrophages as black bars with each data point shown as a gray dot (CR mean diameter = 66.6 nm, CR standard deviation = 2.3 nm, *n* = 257; IR mean diameter = 69.5 nm, IR standard deviation = 7.6 nm, *n* = 247; NR mean diameter = 72.9 nm, NR standard deviation = 3.0 nm, *n* = 224).

(E) For the capsid containing NPC III from Figure 5, an additional computational slice through the NPC in the tomogram is shown with white triangles highlighting the IR subunits (scale bar: 50 nm).

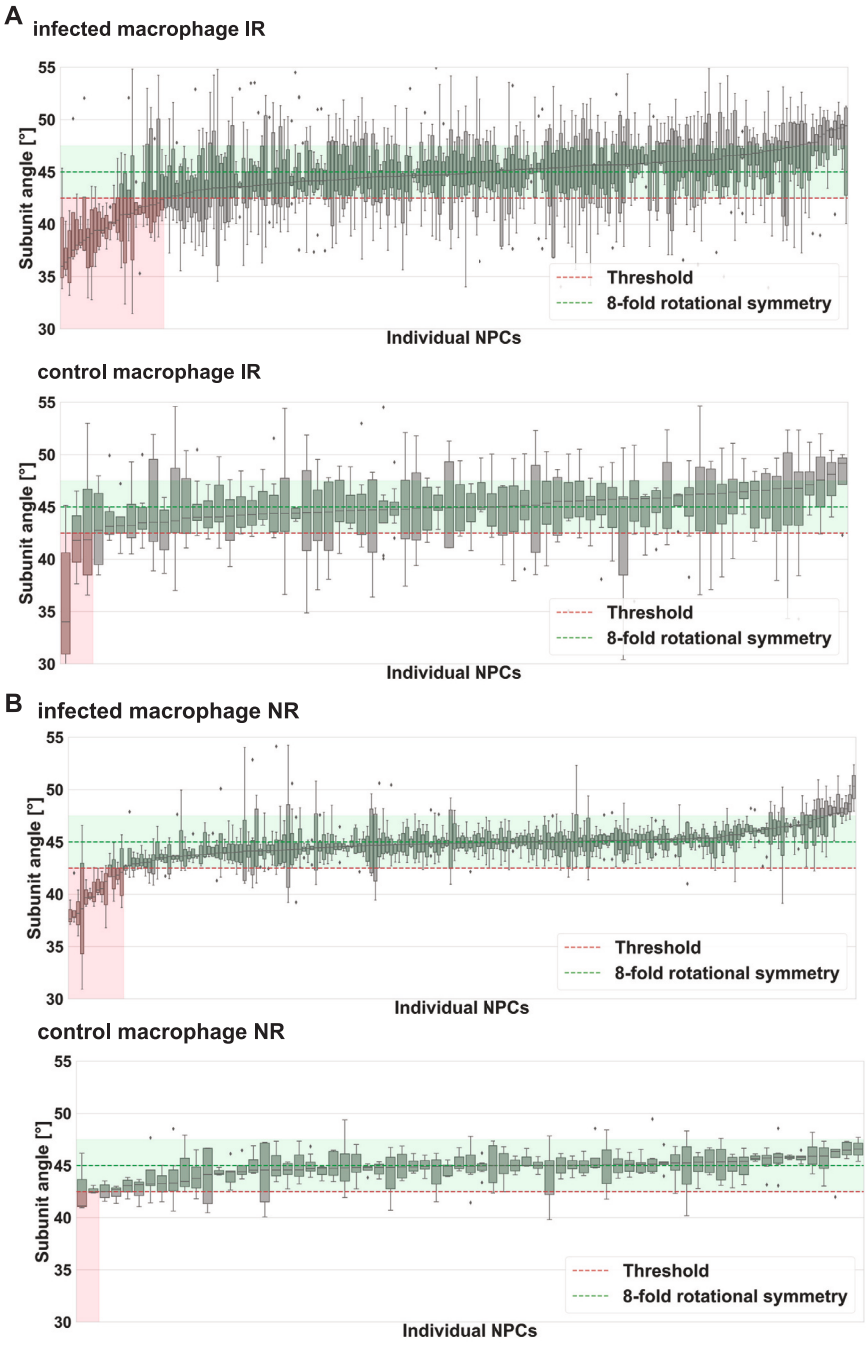

Figure S4. Comparison of IAOP per NPC for the IR and NR of HIV-infected and control macrophages, related to Figure 5

The IAOPs (see STAR Methods) for each ring are plotted as boxplots, and the rings are sorted by median IAOP. A threshold of 42.5° was chosen for the median IAOP, and rings with a median below that value are shown in a red transparent box. An expected range of subunit angles for regular C8-symmetric rings is shown in green transparent box (42.5°–47.5°).

(A) For infected macrophage IRs, there were 185 C8-symmetric and 28 cracked open rings, and for control macrophages, there were 69 C8-symmetric and three cracked open rings (Fisher's exact test, $p = 0.0464$).

(B) For infected macrophage NRs, there were 185 C8-symmetric and 14 cracked open rings, and for control macrophages, there were 67 C8-symmetric and two cracked open rings (Fisher's exact test, $p = 0.3746$).

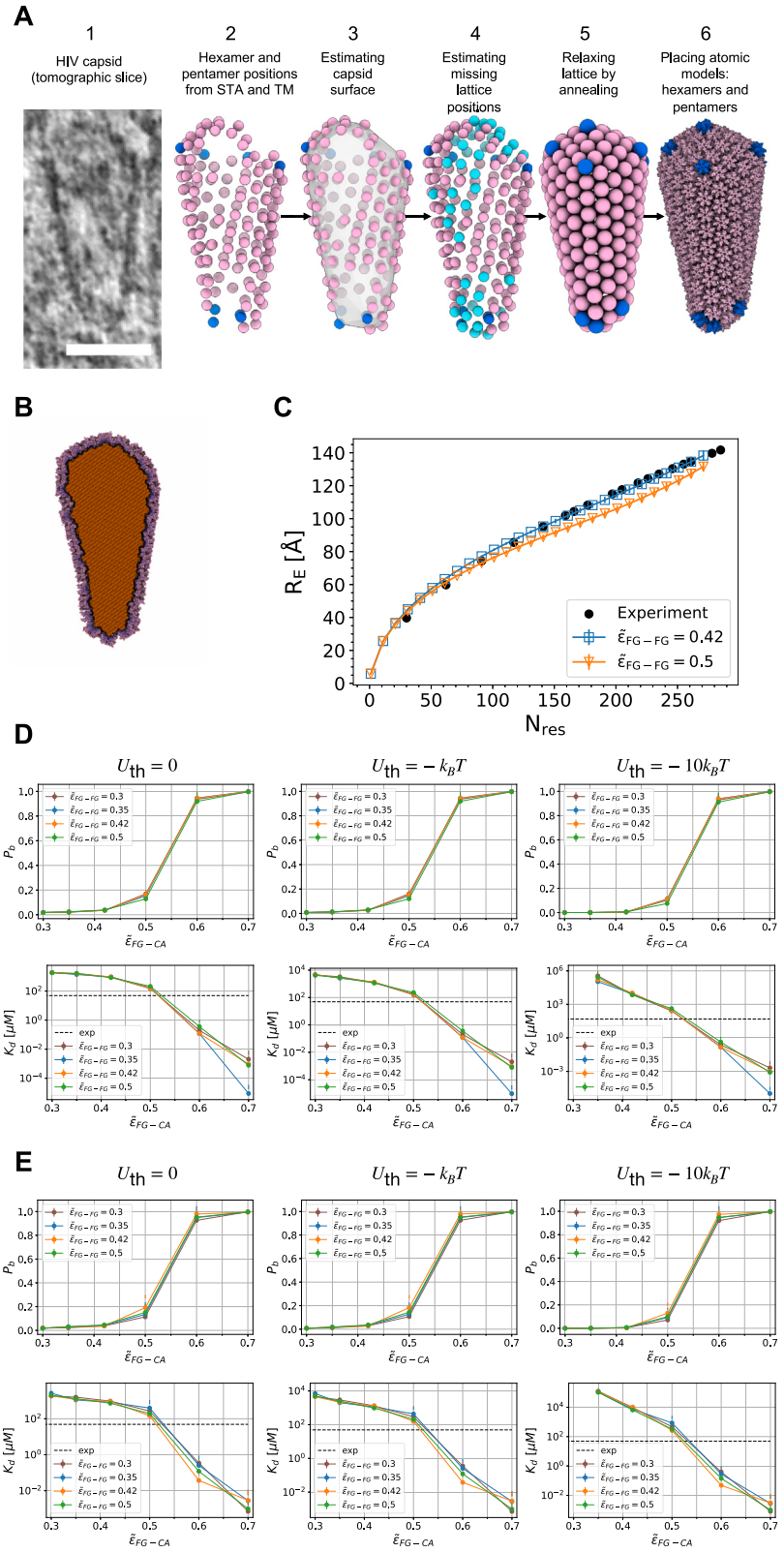

(legend on next page)

Figure S5. Modeling of HIV-1 capsid from *in situ* cryo-ET data, related to Figure 6

(A) (1) Tomographic slice of exemplary cone-shaped capsid (white scale bar: 50 nm). (2) The starting positions of the majority of hexamers (pink) were obtained from STA, and the starting positions of the majority of pentamers (blue) from TM (see STAR Methods). (3) The capsid surface was estimated with the ArtiaX[62] boundary model fit. (4) The positions of the missing hexamers and pentamers (turquoise) were estimated in an iterative process (see STAR Methods). (5) The lattice was relaxed by annealing a coarse-grained particle model. (6) Atomic models of hexamers (PDB: 8ckv[83]) and pentamers (PDB: 8g6l[84]) were placed according to the coarse-grained lattice.

(B) Cut view of HIV capsid filled with lattice particles (orange) ordered on a cubic lattice. The interacting outer surface is shown in dark violet and the inner surface in light violet.

(C) Root-mean-squared (RMS) extension of FG-Nup98 chains inside dilated NPC as a function of separation along the sequence. For interaction strength $\tilde{\epsilon}_{FG-FG} = 0.42$ (blue), the RMS extension of FG-Nup98 chains agrees with the FLIM-FRET distance measurements shown as black spheres.[44] For $\tilde{\epsilon}_{FG-FG} = 0.5$ (orange), the chains are too compact. The symbols and error bars show the average and SEM estimated from four blocks of an MD simulation of $88\times10^3\tau$ duration.

(D am E) Binding probability P_b (top) of FG-Nup153 (1,407–1,423) to CA hexamers and the corresponding dissociation constant K_d (bottom) as functions of their cross-interaction strength $\tilde{\epsilon}_{FG-CA}$ for different values of the FG-FG interaction strength $\tilde{\epsilon}_{FG-FG}$. Results were obtained from MD simulations with Langevin damping coefficients 10τ (D) and τ (E) for binding energy thresholds of $U_{th} = 0$ (left column), $U_{th} = -k_BT$ (middle column), and $U_{th} = -10k_BT$ (right column). For $\tilde{\epsilon}_{FG-CA} \approx 0.5$, the simulation binding affinity matches with the experimental value $K_d^{exp} = 49\ \mu$M (dashed horizontal line[17]).

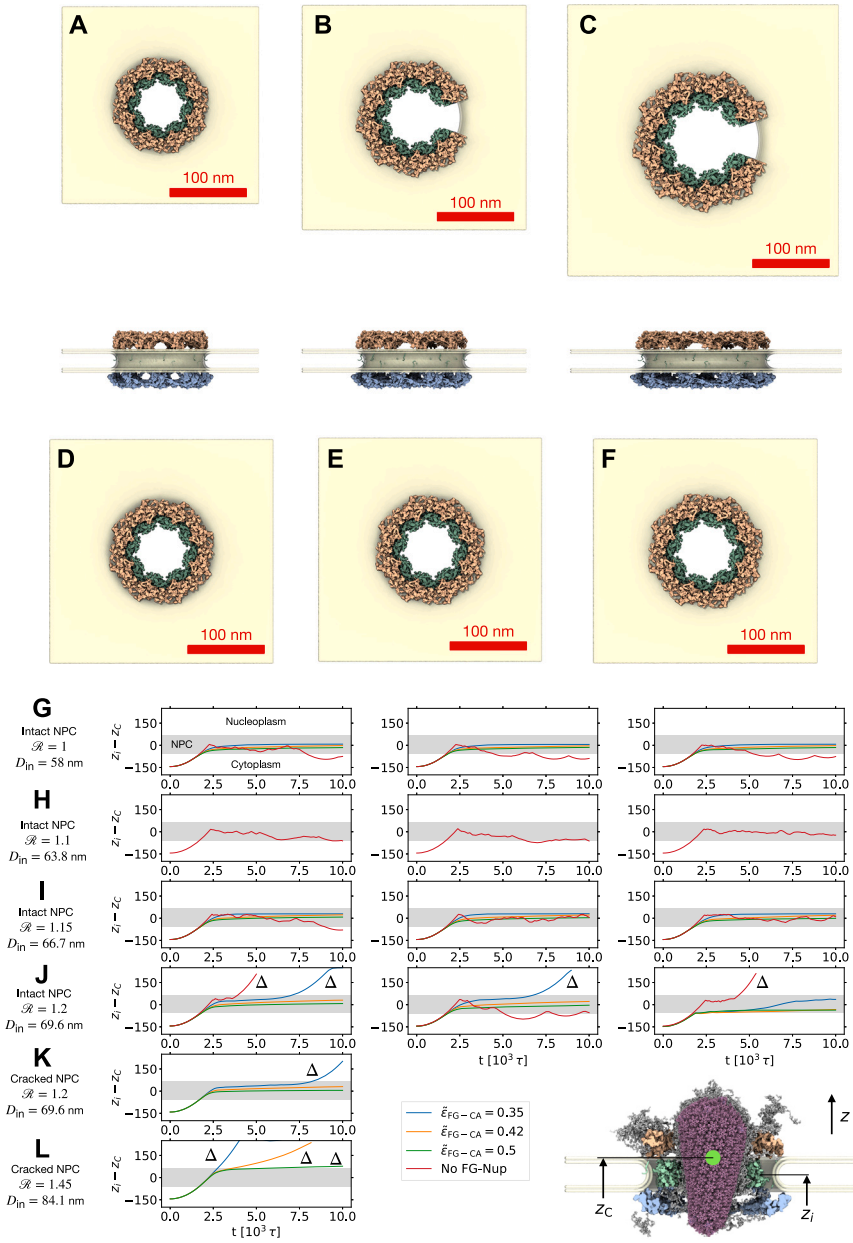

Figure S6. Passage of HIV capsid through intact, cracked, and intact-dilated NPC scaffolds, related to Figure 6

(A–F) Structure of intact NPC scaffold (A, inner-ring diameter D_{in} = 58 nm for scale factor $\mathcal{R}$ = 1), cracked NPC scaffolds (B, D_{in} = 69.6 nm, $\mathcal{R}$ = 1.2; C, D_{in} = 84.1 nm, $\mathcal{R}$ = 1.45), and intact-dilated NPC scaffolds (D, D_{in} = 63.8 nm, $\mathcal{R}$ = 1.1; E, D_{in} = 66.7 nm, $\mathcal{R}$ = 1.15; F, D_{in} = 69.6 nm, $\mathcal{R}$ = 1.2) as seen from the cytosol (top) and the side (bottom). The CR, IR, and NR of the NPC scaffold are shown in orange, green, and blue, respectively, and the nuclear envelope in yellow. (G–L) Passage of HIV capsid through NPC scaffold in MD simulations without FG-Nups (red lines) and with FG-Nups for different interaction strengths (blue, orange, and green lines for $\tilde{\epsilon}_{FG-CA}$ = 0.35, 0.42, and 0.5, respectively). The HIV capsid center positions $z_i - z_C$ (inset at bottom right) are shown as function of time for the intact in-cell NPC (G, D_{in} = 58 nm, $\mathcal{R}$ = 1), the intact-dilated NPC (H, D_{in} = 63.8 nm, $\mathcal{R}$ = 1.1), the intact-dilated NPC (I, D_{in} = 66.7 nm, $\mathcal{R}$ = 1.15), the intact-dilated NPC (J, D_{in} = 69.6 nm, $\mathcal{R}$ = 1.2), the cracked NPC (K, D_{in} = 69.6 nm, $\mathcal{R}$ = 1.2), and the cracked NPC (L, D_{in} = 84.1 nm, $\mathcal{R}$ = 1.45). In (G)–(J), three initial conditions were tested (replicas #1–3) with the capsid rotated around its major axis by 30°. In (K) and (L), one replica was sufficient to demonstrate that the cracked NPC scaffold is permeable to the HIV capsid. Triangles (Δ) indicate successful capsid translocation events. The position of the NPC scaffold is indicated with horizontal gray shade.

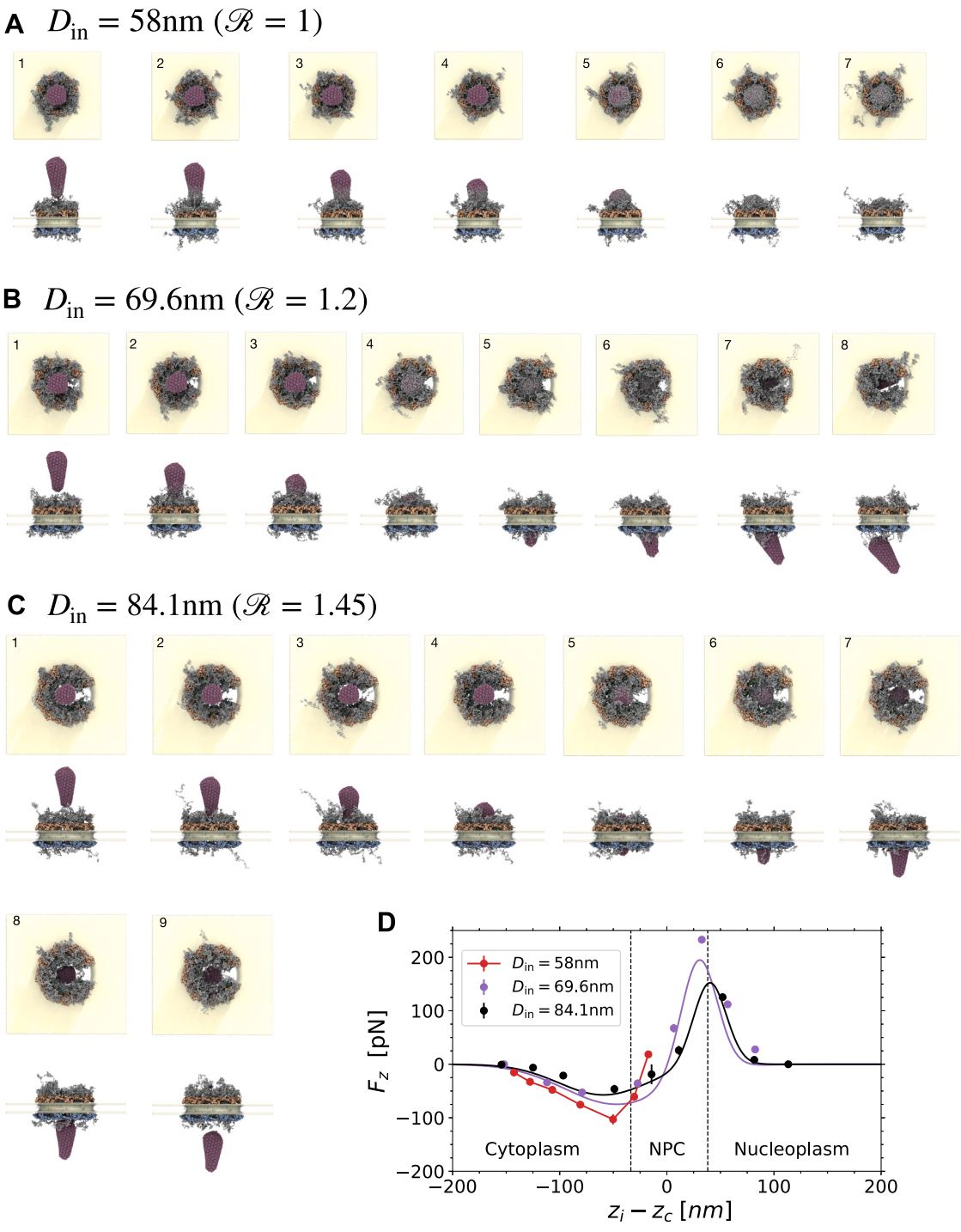

Figure S7. Free energy of HIV capsid passage through NPCs filled with FG-Nups, related to Figure 6

(A) Snapshots showing final configuration in MD simulations of the intact NPC (D_{in} = 58 nm) for different HIV capsid center positions relative to the inner ring of the NPC, $z_i - z_C$ = − 142.7 nm (1), − 127.7 nm (2), − 106.9 nm (3), − 80.8 nm (4), − 50.2 nm (5), − 30.5 nm (6), and − 17.2 nm (7). The interaction strengths were $\tilde{\epsilon}_{FG-FG}$ = 0.42 and $\tilde{\epsilon}_{FG-CA}$ = 0.5. The CR, IR, and NR of the NPC scaffold are shown in orange, green, and blue, respectively, the nuclear envelope in yellow, and the FG-Nups in gray.

(B) Snapshots showing final configurations of MD simulations for different HIV capsid center positions in cracked NPC (D_{in} = 69.6 nm, $\mathcal{R}$ = 1.2): $z_i - z_C$ = − 151.9 nm (1), − 111.8 nm (2), − 79.1 nm (3), − 27.3 nm (4), 6.4 nm (5), 32.6 nm (6), 56.7 nm (7), and 82.3 nm (8). The interaction strengths were $\tilde{\epsilon}_{FG-FG}$ = 0.42 and $\tilde{\epsilon}_{FG-CA}$ = 0.5.

(legend continued on next page)

(C) Snapshots showing final configurations of MD simulations for different HIV capsid center positions in cracked NPC ($D_{in} = 84.1$ nm, $\mathcal{R} = 1.45$): $z_i - z_C = -154.3$ nm (1), -124.9 nm (2), -96.7 nm (3), -49 nm (4), -14.2 nm (5), 11.1 nm (6), 52 nm (7), 81.5 nm (8), and 113.3 nm (9). The interaction strengths were $\tilde{\epsilon}_{FG-FG} = 0.42$ and $\tilde{\epsilon}_{FG-CA} = 0.5$.

(D) Mean force on HIV capsid exerted by FG-Nups and NPC scaffold. The mean force on the HIV capsid at different penetration depths $z_i - z_C$ is shown for the intact in-cell NPC scaffold ($D_{in} = 58$ nm, $\mathcal{R} = 1$: red with lines as guide to the eye). For the cracked NPCs ($D_{in} = 69.6$ nm, $\mathcal{R} = 1.2$: violet; $D_{in} = 84.1$ nm, $\mathcal{R} = 1.45$: black), the solid lines are two-Gaussian fits with a symmetry constraint to ensure that the difference in the potential of mean force obtained by integration across the NPC is zero. For the intact in-cell NPC (red), the HIV capsid collides with the NPC scaffold, which sterically blocks passage, as indicated by the sharp rise in force. The symbols and error bars are the mean and SEM estimated from four blocks of $22.5 \times 10^3 \tau$ each. The final configurations of the systems at different positions of the HIV capsid center are shown in (A)–(C). The HIV capsid was fixed during the mean-force simulations.